Journal of Energy Storage 73 (2023) 109107

Contents lists available at ScienceDirect

Journal of Energy Storage

journal homepage: www.elsevier.com/locate/est

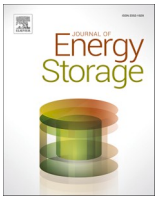

Research Papers

Energy analysis of a lithium-ion battery module for an e-bus application under different thermal boundaries

Alberto Broatch [a,*], Pablo Olmeda [a], Xandra Margot [a], Luca Agizza [a], Manuel Fernández [b]

[a] CMT – Motores Térmicos, Universitat Politècnica de València, Camino de Vera s/n 46,022, Valencia, Spain
[b] FTM – Fluid & Thermal Management, Ronda Narciso Monturiol y Estarriol, 19 – Parque Tecnológico de Valencia, 46,980. Paterna (Valencia), Spain

ARTICLE INFO

Keywords:
lithium-ion
Cooled battery module
Experimental characterization
Electro-thermal modelling
Fast charging parametric study
Cooling system design

ABSTRACT

In this study, a methodology for the energy analysis of a lithium-ion battery module cooled by a serpentine cooling plate is proposed. A novel lumped electro-thermal model of a cooled module is calibrated and validated: thermal nodes are assigned to the Li-ion cells, the cooling plate, the thermal pad, and the coolant. The model is experimentally characterized and validated, and a maximum root mean square error equal to 1.44 % for the electrical model is obtained; all the errors of the thermal models are kept below the 2 %. The proposed approach allows to identify, with a low computational cost and reduced calculation time, the thermal evolution of the nodes depending on the environmental and operating conditions considered. This aspect is of fundamental importance to identify hot spots in the module and to prevent possible dangerous events such as thermal runaway. To highlight these advantages, an extended fast-charging parametric study of the module is carried out, considering 240 simulations, varying 4 parameters (ambient temperature, required electric power, temperature and coolant volumetric flow) and monitoring 3 variables (peak temperature in the module at the end of the charging process, thermal gradient, and time spent in the optimal temperature range), allowing to identify the combinations of operating parameters that permit the rapid charging of the module under optimal conditions. Furthermore, the energy analysis provides an estimation of the charging efficiency of the cells, which is around 90 % for every considered thermal boundary. The heat generated by the cells, the heat dissipated into the coolant and the heat absorbed by the other module components are estimated. In a 4C charge 80 % of total heat is dissipated into the coolant, while this quantity increases to 95 % in a 1C charge. The reduced computational time and cost make this model suitable both for cooling system design and for control strategies development.

List of symbols

Symbols	Description
A	area, m^2
c_i	specific heat of ith node, $J \bullet kg^{-1}K^{-1}$
C_{th}	thermal capacity of the lithium-ion cell, $J \bullet K^{-1}$
C_{Ah}	measured capacity, Ah
C_1	double layer capacitance, F
C_n	nominal capacity at T_{ref}, Ah
$\overline{C_T}$	Average measured capacity at temperature T, Ah
C_T^{MAX}	Maximum capacity measured at temperature T, Ah
C_T^{MIN}	Minimum capacity measured at temperature T, Ah
$[C]$	capacitance matrix
D	diameter of the cell, m
d	distance, m
E_{stored}	Energy stored in the cells during charging, Wh

(*continued on next column*)

(*continued*)

Symbols	Description
$E_{provided}$	Electrical energy provided for the module charging, Wh
h	Heat transfer coefficient, $W \bullet m^{-2}K^{-1}$
I	electrical current, A
L	length of the cell, m
k_a	thermal conductivity in the axial direction, $W \bullet m^{-1}K^{-1}$
k_r	thermal conductivity in the radial direction, $W \bullet m^{-1}K^{-1}$
$[K]$	Conductance matrix
m_i	mass of ith node, kg
$\dot{m}_{wg}$	mass flow of the water-glycol mixture, kg/s
N_{cells}	Total number of the cells in the module
Nu	Nusselt number
Δp	pressure drop, bar
P_{batt}	battery power, W
Q_d	Heat dissipated by the cells, Wh

(*continued on next page*)

* Corresponding author.
E-mail address: abroatch@mot.upv.es (A. Broatch).

https://doi.org/10.1016/j.est.2023.109107
Received 16 June 2023; Received in revised form 7 September 2023; Accepted 27 September 2023
Available online 6 October 2023
2352-152X/© 2023 The Authors. Published by Elsevier Ltd. This is an open access article under the CC BY-NC-ND license (http://creativecommons.org/licenses/by-nc-nd/4.0/).

(*continued*)

Symbols	Description
Q_{abs}	Heat absorbed by the cells, Wh
Q_g	Heat generation of the cells, Wh
$\dot{Q}_g$	Heat generated by the cells, W
Pr	Prandtl number
R_0	ohmic resistance, Ω
R_1	charge transfer resistance, Ω
R_k	conductive resistance, K/W
R_c	convective resistance, K/W
R_{x-y}	conductive resistance between two module components, K/W
R_{wg}	conductive resistance between contiguous coolant nodes, K/W
$R_{el,tab}$	Electric resistance of the connection plate, Ω
r	cell radius, m
s_p	calibration parameter for pressure drops regression model
T	temperature, K
t	time, s
Δt_{1-2}	pulse duration, s
th_{tab}	thickness of the electrical connection, m
v	voltage, V
$\dot{V}_f$	volumetric flow of the coolant, m^3/s
Subscripts	
0	Beginning of the process
air	Air surrounding the cells
c	Coolant
cell	Lithium-ion cell
end	End of the process
foam	Thermal pad between cell and cold plate
plate	Cold plate
surf	Surface
tab	Electrical connection between cells
wg	Water-glycol
Greek letters	
η	coulombic efficiency
ξ	electrical resistivity, Ωm
μ	dynamic viscosity, m^2/s
ρ	density, kg/m^3
Acronyms	
BMS	Battery management system
BEV	Battery Electric Vehicle
CCCV	Constant Current Constant Voltage
CFD	Computational fluid dynamics
ECM	Equivalent Circuit Model
HEV	Hybrid Electric Vehicle
HPPC	Hybrid Pulse Power Characterization
LFP	Lithium iron phosphate
OCV	Open circuit voltage
PEV	Plug-in Electric Vehicle
RMSE	Root Mean Square Error
SOC	State of charge

1. Introduction

Electrified vehicles (BEV, PEV, HEV) are massively spreading in the last years due to recent regulations at European [1] and international level [2]. This conversion of the automotive fleet is aimed to reduce pollutants and emissions from vehicles [3]. Electrified vehicles have been recognized as one of the possible solutions to this problem, even though, in order to reduce global emissions significantly, a conversion of the electricity production system to renewable energy sources is needed [4]. Apart of the cars, also buses, lorries and boats are transitioning to electrified powertrains [5]. Therefore, there is a huge need for developing solutions to the different applications in which an electrified powertrain is used. The component which needs the major development efforts is the lithium-ion battery [6]. Some of the major issues of this component are related to the thermal management [7] and to the fast charging [8]. A lithium-ion battery, in fact, is supposed to work properly only in a limited range of temperatures [9]. A thermal management system should avoid that the battery works neither under extremely high temperatures [10], at which thermal runaway can occur, nor at very low temperatures, at which other problems, such as the formation of dendrites [11] and the capacity loss and resistance increase may worsen the performance and create danger [12]. To improve the solutions to these problems and get a better understanding of the thermal issues of a lithium-ion battery, it is fundamental to develop electro-thermal models able to provide a sufficiently precise description of the mechanisms of heat generation inside a lithium-ion cell and of its propagation and transfer inside the cell itself and among the different cells of a lithium-ion battery pack [13]. Two main categories of battery models are discussed in the literature: physical electro-chemical models need a deep understanding of the mass transport, electrochemistry and diffusion phenomena occurring inside the cells and may provide a precise description of the phenomena, nut at the cost of a high calculation time and the need to calibrate many parameters [14]; lumped electro-thermal models, generally based on analogies (ECMs or nodal networks are based on analogies with electrical circuits) are characterized by lower calculation times and less calibration parameters, but they need generally more testing for determination of lumped parameters [15]. Due to their relative easiness of use and computation speed, lumped models can be more adequately integrated into the battery management system temperature control strategies for on-line temperature estimation.

In the literature, plenty of models of lithium-ion battery modules are available. Nonetheless, while many lumped thermal models are available for a stand-alone cell, most module/battery thermal models in the literature are 3D/CFD based. Li et al. [16] proposed a three-dimensional electrochemical-thermal model to describe the thermal evolution of battery packs. Free and forced air convection cooling systems were compared by employing a CFD model. This methodology needs a CFD software to solve the governing equations. Morali [17] analyzed the effect of several parameters (temperature, discharge rate, depth of discharge, heat transfer coefficient) on the thermal evolution of a battery pack composed by LMO prismatic cells. In this case ANSYS Fluent CFD software was used to solve the multi-scale multi-dimensional governing equations. Once again, the use of CFD software for solving the model equations hugely affected the calculation time and the computational cost. Jiaqiang et al. [18] investigated the thermal evolution of an air-cooled 60-cell battery module. They analyzed different air-cooling strategies by means of a computational fluid dynamics method, finding that the use of a baffle improved the air flow distribution. Akbarzadeh et al. [19] analyzed a 12-cell prismatic module by using a 3D thermal model at room temperature. In this case, the authors also used a lumped thermal network and a three-dimensional thermal model at different environment temperatures, but no analysis of the coupling with a thermal management system was presented. Saw et al. [20] analyzed a battery pack composed of 24 cylindrical cells. They used a computational fluid dynamics model to analyze the thermal evolution of the module coupled with an air-cooling system, evaluating the refrigeration capability of the thermal management system at different charging rates. Bahiraei et al. [21] proposed a 3D electrochemical-thermal model aimed to understand the impact of several design and operating parameters on a battery module composed by 6 prismatic cells. All the governing equations were solved by using the Finite Elements Method (FEM) in COMSOL software. Zhao et al. [22] studied the thermal behavior of a lithium-ion battery module during charging/discharging phases by means of a computational fluid dynamics model. The aim of their analysis was to investigate the effect of the charge/discharge rate, the liquid flow rate, the heat exchange area and the interfacing of the cells with the side cooling plate.

The novelty of this work consists in the fact that a complete lumped methodology for battery module characterization is proposed: the lumped thermal nodal network representation is used to describe not only the stand-alone cell thermal behavior, but also the whole battery module thermal behavior. This approach is very different from most of the models proposed in literature which either use 3D/CFD approach both for cell and module level thermal characterization or they use lumped thermal model only at cell level, keeping the 3D/CFD representation at module level. These differences between the proposed

model and the ones available in literature are summarized in Table 1.

The major novelties of the proposed model can be summarized as follows:

- there is a single thermal nodal network which represents the thermal evolution of all the solid components of the module, which are not only the cells, but also the electrical connections, the thermal contact foam, and the cooling plate.
- the model also assigns nodes to each coolant: nodes are assigned to the air surrounding the cells (allowing to calculate the heat, even though minimal, that is dissipated in the air) and other nodes are assigned to the refrigerant coolant (allowing to calculate the heat dissipated in the cooling system).
- the model is totally independent from other external models, and once the inputs have been assigned (coolant temperature T_f, ambient temperature T_{amb}, volumetric flow $\dot{V}_f$, power demand P_{batt}), and the parameters (thermal and electrical parameters, previously determined through testing campaign), it allows calculating the thermal evolution of a battery module when varying power demand and conditions of the refrigeration circuit.

These characteristics allows to use this model either for design studies (once fixed the power demand of the module, the temperature and mass flow of the coolant can be determined to make the module operates within the optimal temperature range), or for control strategies, due to its relatively low computational time and easiness of the calibration process.

Heat generation is assigned to the cells: this is calculated thanks to the parameters which have been calibrated in the experimental campaign. Heat generation has been assigned also to the electrical connections using the electrical resistivity of the material and the dimensions of this component. Since the proposed lumped model describes the whole module coupled with its thermal management system, this aspect makes it suitable not only for off-line studies, but also for integration into BMS temperature control strategies (on-line use). In this paper, a thermal analysis of the module is proposed: by varying the volumetric flow and the temperature of the coolant, the ambient temperature, and the charging rate. The goal of the analysis is to determine under which conditions, during a fast-charging event, the module can work properly in the optimal range of temperature, what is the temperature achieved, which are the hot spots and what spatial temperature differences are induced inside the module.

This work is divided into seven sections: after this introduction, Section 2 is dedicated to the description of the experimental tools; Section 3 describes the numerical tools developed in this study; Section 4 deals with the experimental campaign carried out in order to determine the model parameters; Section 5 discusses the validation of the model; Section 6 describes the parametric study carried out in order to understand the thermal performance of the module; and Section 7 is dedicated to the conclusions.

Table 1
Models comparison.

Work	Cell electric model	Thermal model: cell level	Thermal model: module level
Broatch et al. (present work)	ECM 1st order	Lumped thermal model	Lumped thermal model
Li et al. [16]	Electrochemical single particle model	3D Model (Comsol Multi-physics 5.5)	3D Model (Comsol Multi-physics 5.5)
Morali et al. [17]	NTGK semi-empirical model	3D CFD ANSYS CFX	3D CFD ANSYS CFX
Jianqiang et al. [18]	ECM 1st order	Lumped thermal model	3D CFD ANSYS FLUENT
Akbarzadeh et al. [19]	Measurement of OCV and voltage at different T and SOC	Lumped thermal model	3D CFD ANSYS FLUENT
Saw et al. [20]	Measurement of heat generation in the calorimeter	3D CFD ANYS FLUENT	3D CFD ANSYS FLUENT
Bahiraei et al. [21]	Electrochemical model: porous electrode theory	3D Model (Comsol Multi-physics 5.2)	3D Model (Comsol Multi-physics 5.2)
Zhao et al. [22]	Electrochemical model	Lumped thermal model	3D CFD ANSYS FLUENT

2. Experimental tools

A cylindrical lithium-ion cell has been characterized in this work. The main characteristics of the cell are listed in Table 2.

The cell has been tested in order to calibrate its internal parameters. The battery tester used for the charge/discharge process is an Arbin battery cycler with 4 channels, each of them providing 100 A and 10 V. The control of ambient temperature is achieved with a thermal chamber from Espec. Data was recorded with a datalogger, and temperature was measured with K-type thermocouples applied on the surface and terminals of the cells. The cell was held during testing activities by a holder realized in-house. The test bench composed by the Arbin tester and the Espec thermal chamber is shown in Fig. 1.

Another test bench was devised to characterize the cold plate designed for the cooling of the battery module. The cold plate used for this application is shown in Fig. 2 and its characteristics are listed in Table 3.

This test bench, as Fig. 3 shows, is composed by the following elements:

- A water pump, to override pressure losses and produce the mixture of water and refrigerant flow through the installation.
- A Krohne Optiflux 4000 DN15 electromagnetic flowmeter to measure the refrigerant flow.
- A 4500 W resistor to heat the refrigerant when necessary and a PID (RKC REX-AC110 model) to regulate the power to be supplied to the resistor.
- A shell and tubes heat exchanger to cool the refrigerant coolant from the cooling plate.
- A chiller as a cold source connected to the previously mentioned.

Finally, a summary of the estimated uncertainties associated with typical measurement values is presented in Table 4, both for the electrical and for the hydraulic test bench.

3. Numerical tools

In this work a model of a cylindrical cell module cooled with a coil-type cold plate is proposed. Every cell is electrically modeled with an independent ECM; then, the heat generated by each cell is given as an input to the thermal nodal network (TNN). The TNN model calculates the temperature of each element and gives back to each ECM the cell temperature that will be used to calculate the new value of electrical

Table 2
32,700 cylindrical lithium-ion cell.

Characteristic	Value
Nominal Capacity	6 Ah
Nominal Voltage	3.2 V
Maximum Voltage	3.65 V
Minimum Voltage	2 V
Diameter	32 mm
Length	70 mm
Cathode/Anode Chemistry	LFP/Graphite
Discharge temperature	[−10 60] °C
Charge temperature	[0 45] °C

Fig. 1. Test bench for battery cell characterization.

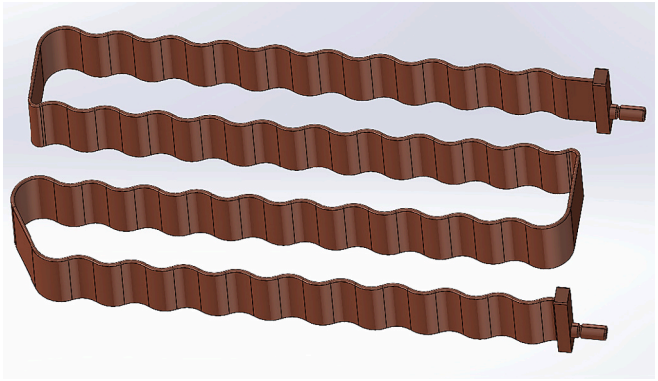

Fig. 2. Cold plate used for module refrigeration.

Table 3
Cold plate characteristics.

Characteristic	Value
Wall Thickness	2.4 mm
Width	0.45mm
Height	47.6 mm
Material	Aluminum

parameters, and this is repeated until the simulation finishes. The structure of the model is shown in Fig. 4.

3.1. Cell electro-thermal model

The electrical behavior of the cell is described with an equivalent circuit model, show in Fig. 5. This type of model describes the cell based on an analogy with an electrical circuit where the input is the electric current and the output is the voltage across the cell terminals. The advantage of using this type of model consists in the fact that it is sufficient to calibrate a few parameters experimentally, and a deep knowledge of electrochemical, diffusion and mass transport phenomena is not required. In this work a first order equivalent circuit model has been calibrated [24].

In this model, 4 parameters need to be calibrated:

- The open circuit voltage $OCV = f(SOC)$: this parameter represents the voltage delivered by the cell when it is idle and it has been estimated running quasistatic open circuit voltage tests at different temperatures. The results of the characterization of this parameter will be presented in Section 4.

The state of charge of the cell is estimated according to coulombic counting method, as follows [25]:

$$SOC = SOC_0 - \frac{1}{C_{Ah}} \int_{t_0}^{t} \eta I dt \quad (1)$$

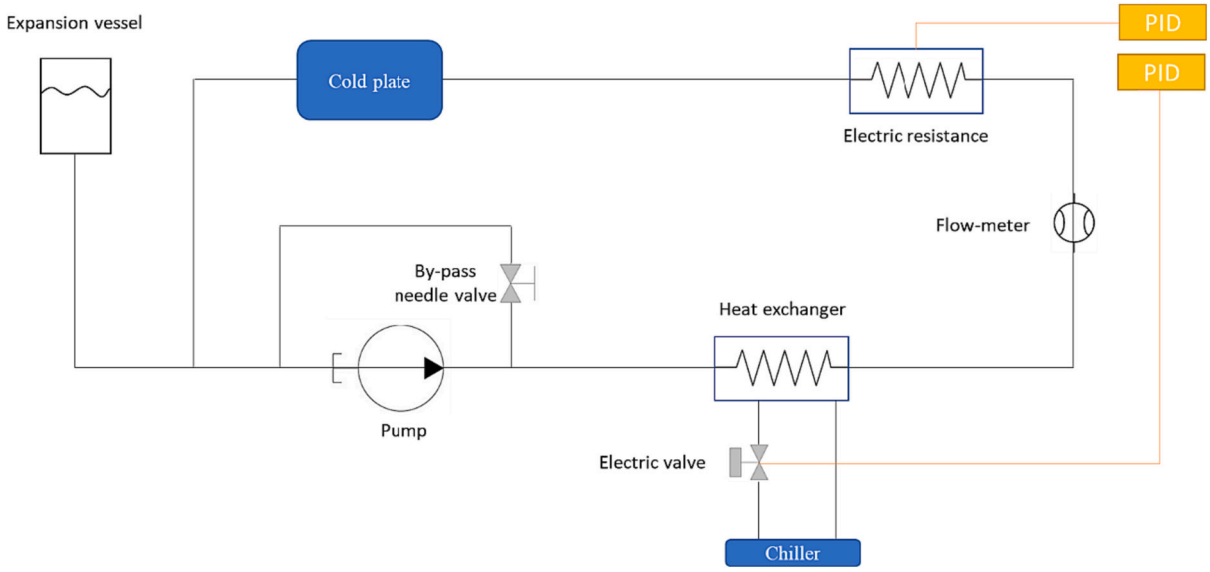

Fig. 3. Test bench for cold plate characterization.

Table 4
Uncertainty of the variables.

Variable	Symbol	Uncertainty σ [%]
Current	I	0.33%
Voltage	v	0.1%
Temperature	T	1.68%
Volumetric flow	$\dot{v}_f$	0.3%
Pressure	p	0.5%

- The ohmic resistance $R_0 = f(SOC, c-rate, T)$ which is a lumped parameter that takes into account the losses due to Joule effect occurring in the different components of a lithium-ion cell, that are the current collectors, the electrodes (anode and cathode) and the separator [26]. This parameter changes with the *SOC*, the temperature and the electrical current: for this reason, it is calibrated through Hybrid Power Pulse Characterization (HPPC) tests repeated at different temperatures as shown in Section 4 [27].
- The charge-transfer resistance $R_1 = f(SOC, c-rate, T)$ which is a lumped parameter that takes into account the losses due to the migration of the ions from the solid phase (electrode) to the liquid phase (electrolyte). This kind of losses are concentrated in the anode and the cathode. As in the case of the ohmic resistance, this parameter has been calibrated through HPPC tests repeated at different temperatures [28].
- The double-layer capacitance $C_1 = f(SOC, c-rate, T)$ which allows to describe the dynamic behavior of the cell and is again calibrated with HPPC tests.

The governing equations of a first order model are the following ones [29]:

$$v(t) = OCV(SOC(t)) - v_c(t) - R_0 I(t) \tag{2}$$

$$\frac{dv_c(t)}{dt} = \frac{1}{C_1}\left(I - \frac{v_c(t)}{R_1}\right) \tag{3}$$

Once the electrical model has been calibrated, it is possible to give an estimation of the heat generation in a lithium-ion cell [23]. In this work, the heat generation has been estimated as in Eq. (4):

$$\dot{Q}_g = I \bullet (v - OCV) \tag{4}$$

The right-hand side of Eq. (4) represents the irreversible heat generated in every component of the cell (current collectors, anode, cathode and separator). The irreversible heat is given by ohmic, activation and concentration polarization. Ohmic polarization is due to charge transport; activation polarization is due to potential difference between actual and equilibrium values; and concentration polarization is due to changes in electrolyte concentration due to ion migration through the electrode/electrolyte interface.

The heat generation is the input of the thermal model. In this work, a nodal network has been proposed to describe the thermal behavior of the cell. The nodal network is represented in Fig. 6 and it is composed of 4 solid nodes: one for the external surface (node 4 in Fig. 6), one for each of the two terminals (node 1 and 3 in Fig. 6) and one for the core (node 2 in Fig. 6). The core node is connected to the other cells nodes through the conductive resistances (R_{k1}, R_{k2}, R_{k3}). A convective heat flux is associated to surface and terminal nodes through convective resistances (R_{c1}, R_{c2}, R_{c3}). Values of density, thermal conductivity and specific heat capacity are assigned to each of the nodes according to the material composition [30]. A volume is assigned to each node in order to calculate its thermal capacitance. Heat generation is assigned to the core node and to the terminals according to the distribution proposed by Nazari et al. in [31].

The governing equation of the thermal model, for a generic node, is obtained from an energy balance in the node as [32]:

$$m_i c_i \frac{T^i_{t+\Delta t} - T^i_t}{\Delta t} = \sum_j K_{ij}\left(T^j_{t+\Delta t} - T^i_{t+\Delta t}\right) + \sum_k \dot{Q}_{k\to i} + \sum_j h_{ij} A_{ij}\left(T_f - T^i_{t+\Delta t}\right) \tag{5}$$

The left-hand side of Eq. (5) considers the heating of the cell node due to its thermal capacity; the first term on the right-hand side of Eq. (5) takes into account the conductive heat transfer with the other solid nodes, while the second term represents the heat generation at the node and the third term represents the convective heat transfer with coolant nodes. This equation is solved with an implicit formulation, which is chosen because it is unconditionally stable. Eq. (5) is applied to each solid and coolant node so that a matrix equation is obtained:

$$[T^t] = ([K] - [C])^{-1}\left([T^{bc}] - [C][T^{t-\Delta t}]\right) \tag{6}$$

3.2. Model of the module coupled with the serpentine cooling plate

A nodal network for the thermal modelling of the module is needed.

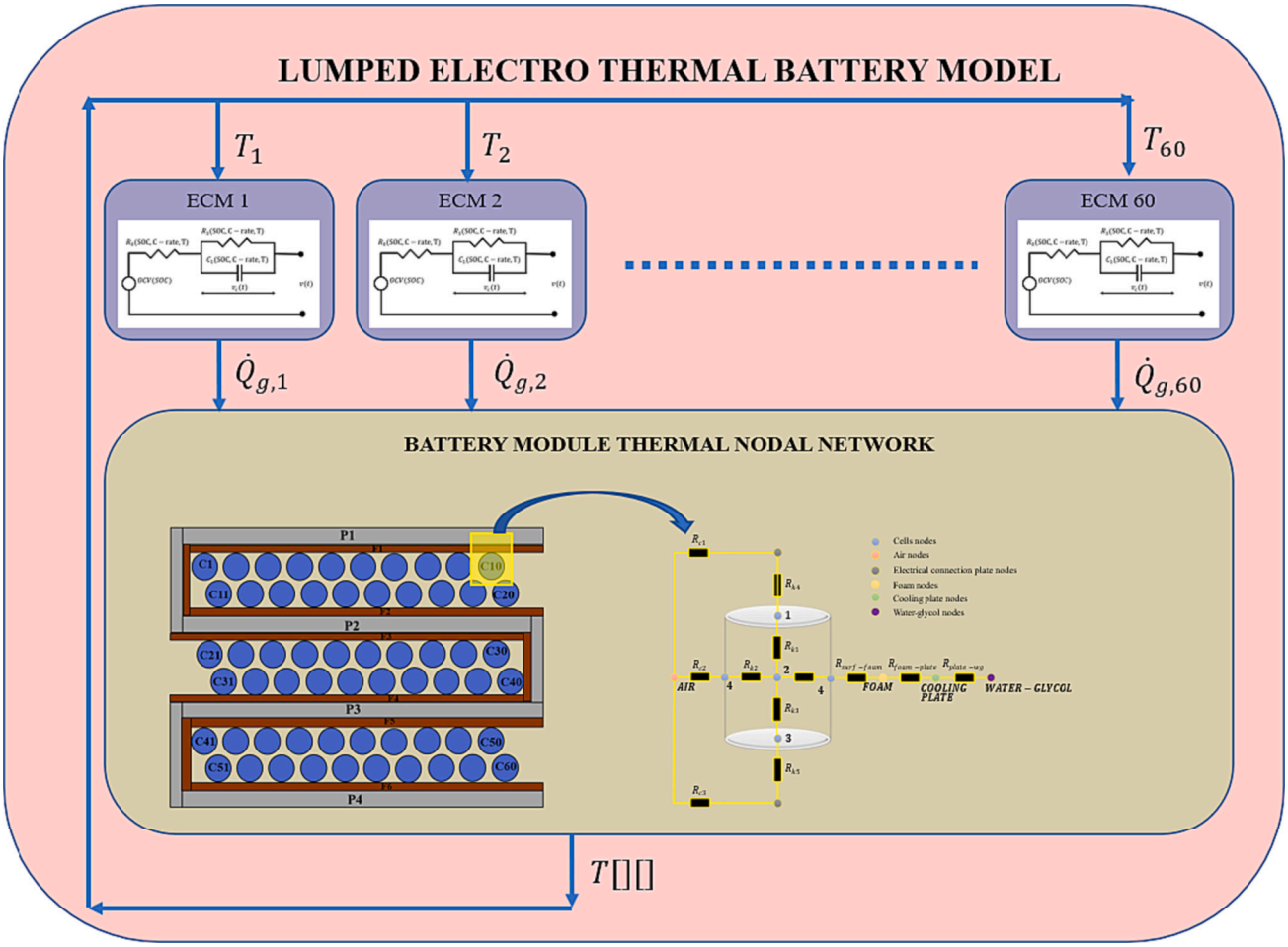

Fig. 4. Structure of the lumped electro-thermal battery module.

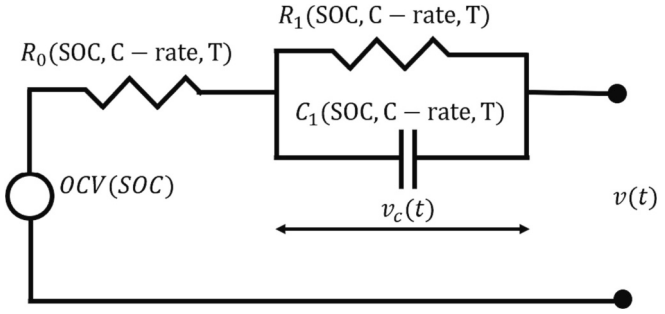

Fig. 5. First order equivalent circuit model.

The components of the module are shown in Fig. 7:

- (a): Upper view of the cells connected in series and parallel and their holders.
- (b): View of the cells and the serpentine cooling plate whose wavy shape guarantees a good contact with the cells surfaces.
- (c): Lower view of the cells connected in series and parallel and their holders.
- (d): Details of the series connection of the cells: the negative terminals of 5 cells are connected to the positive terminals of other 5 cells through a nickel connection plate.
- (e): Detail of the positive terminal of the battery (5 cells on the left side) connected by means of a connection plate to which the power cable will also be connected; the 5 cells on the other side are also

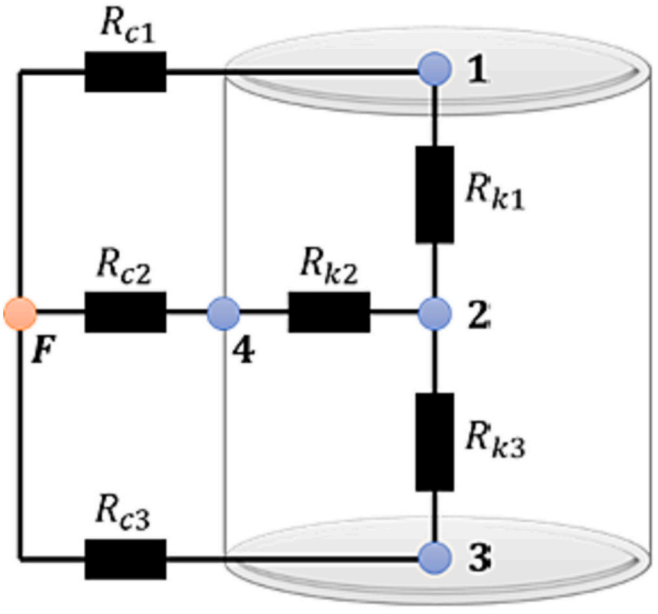

Fig. 6. Nodal network of one cell.

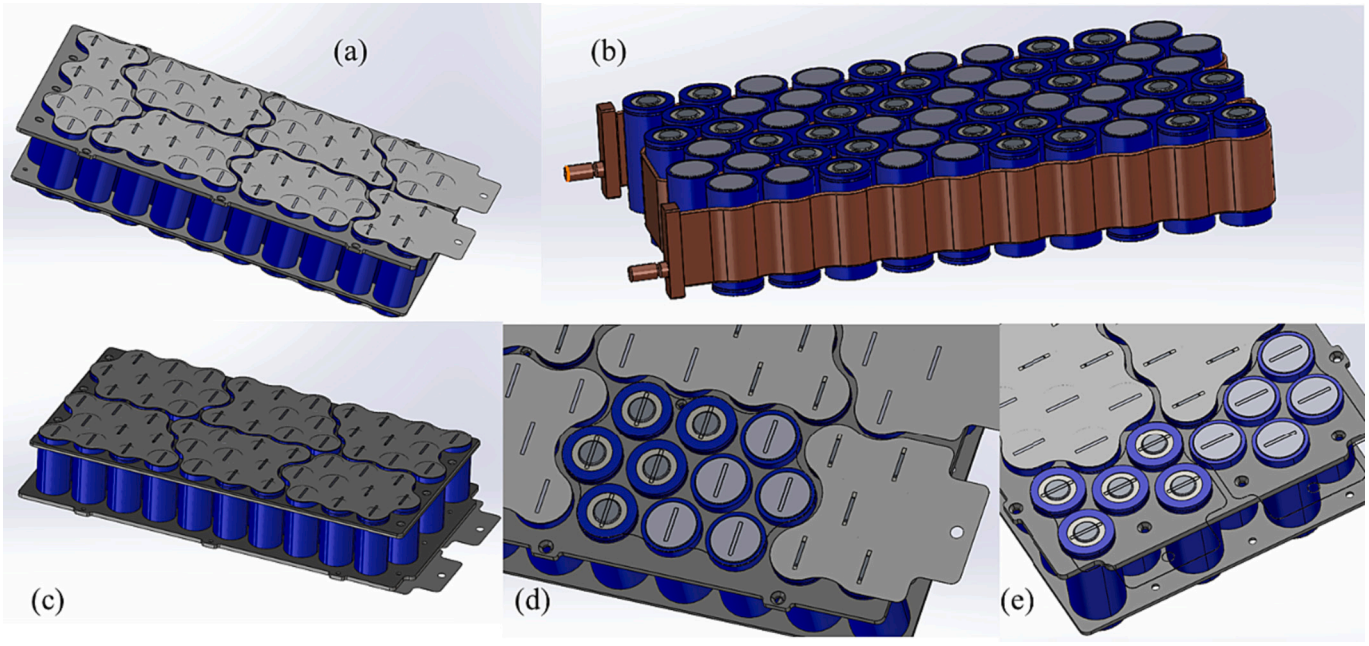

Fig. 7. (a): Upper side of the module; (b): Assembly of the cells with the cooling plate; (c): Lower side of the module; (d): detail of the series connection; (e): detail of the of the positive and negative terminal of the module.

interconnected and they make the negative terminal of the module available to connection with the power cable.

The nodal network for a single cell is represented in Fig. 8 and the whole module is composed by the following elements:

- 60 cells, composing the module, connected electrically with the configuration 12S5P, that is 12 cells in series and 5 in parallel. To each cell, 4 solid nodes are assigned, as explained in the previous sub-section.
- 13 electrical connection plates, whose material is nickel. Through these plates, the electrical connections needed in order to meet power and energy requirements are realized. To each of these plates, 1 node is assigned.
- Foam, to ensure good thermal contact between the lateral surface of the cells and the cooling plate and also to avoid electrical contact between cells and the cooling plate. Foam is discretized into 6 nodes.
- Cooling plate, through which the cooling liquid flows. For the plate a discretization in 4 nodes has been considered.
- Cooling fluid, that is a mixture of water and glycol (50 % glycol). In order to take into account the heating of the coolant due to the heat dissipated by the cells, 4 nodes were assigned to the water-glycol mixture. The glycol comes in at a certain temperature T_c and with a certain volumetric flow $\dot{V}_f$ and then, according to ambient temperature and heat generated, it can heat up or cool down.
- Air surrounding the cells: all the components of the module are covered by a box; nonetheless the model should take into account the little volumes of air between the cells. Therefore, a discretization of the air volume in the battery module has been considered.

Summarizing the previous information, Table 5 shows all the elements considered in this thermal nodal representation with their corresponding number of nodes.

The following aspects were considered for model development:

- Heat convection between each cell in the module and the surrounding air nodes. This convective heat transfer depends on the heat transfer coefficient in free convection with air and on the surface in direct contact with the surrounding air. The convective resistance R_{c2} can be expressed as follows:

$$R_{c2} = \frac{1}{h_{air} A_{surf,air}} \tag{7}$$

- Heat conduction between each cell in the module and the corresponding electrical connection plates at positive and negative terminals. This thermal resistance depends on the thermal conductivity of the materials and the base area of the cells:

$$R_{k4} = R_{k5} = \frac{d_{cell,tab}}{k_{cell,tab} A_{base}} \tag{8}$$

- Heat conduction between each cell and the correspondent foam node, which depends on the surface in contact with the foam and on the thermal conductivity of the materials:

$$R_{surf-foam} = \frac{ln\left(\frac{r_{cell}}{r_{foam}}\right)}{2\pi k_{cell,foam} L} \tag{9}$$

- Heat conduction between each foam node and the correspondent cooling plate node. The conductive resistance depends on mutual heat transfer area and the thermal conductivity of the materials:

$$R_{foam-plate} = \frac{ln\left(\frac{r_{foam}}{r_{plate}}\right)}{2\pi k_{foam,plate} L} \tag{10}$$

- Heat convection between each cooling plate node and the corresponding water-glycol node. This conductive heat transfer depends on the heat transfer coefficient. Calculated employing a heat transfer correlation for forced convection with water-glycol mixtures validated with the results of a computational fluid dynamics code, and on the heat transfer area:

$$R_{plate-wg} = \frac{1}{h_{wg} A_{plate,wg}} \tag{11}$$

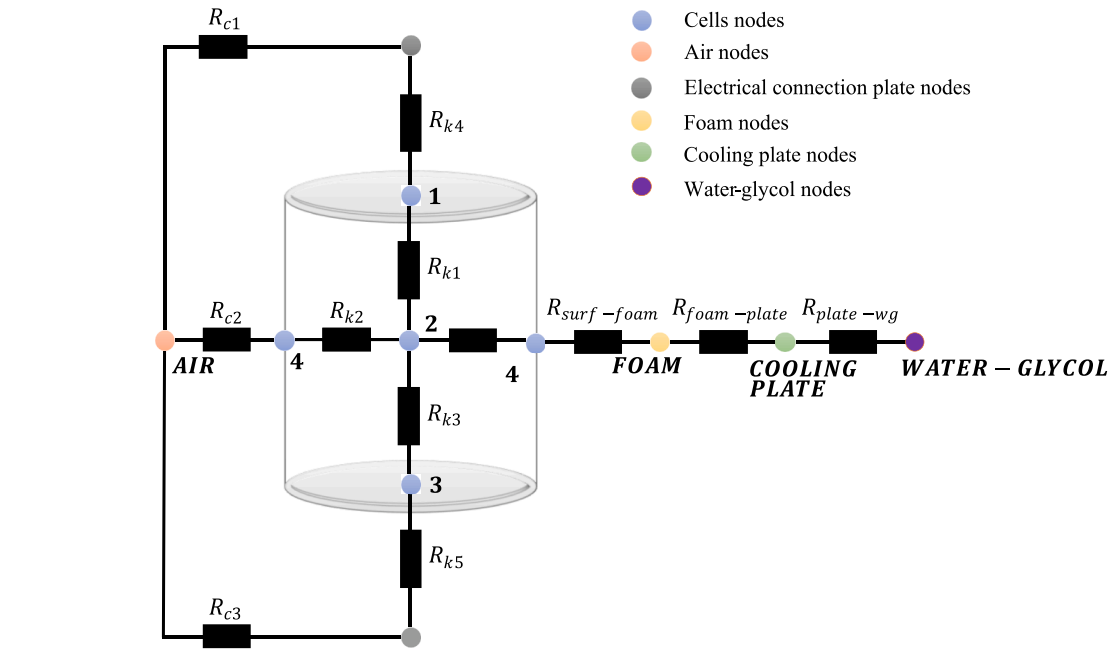

(a)

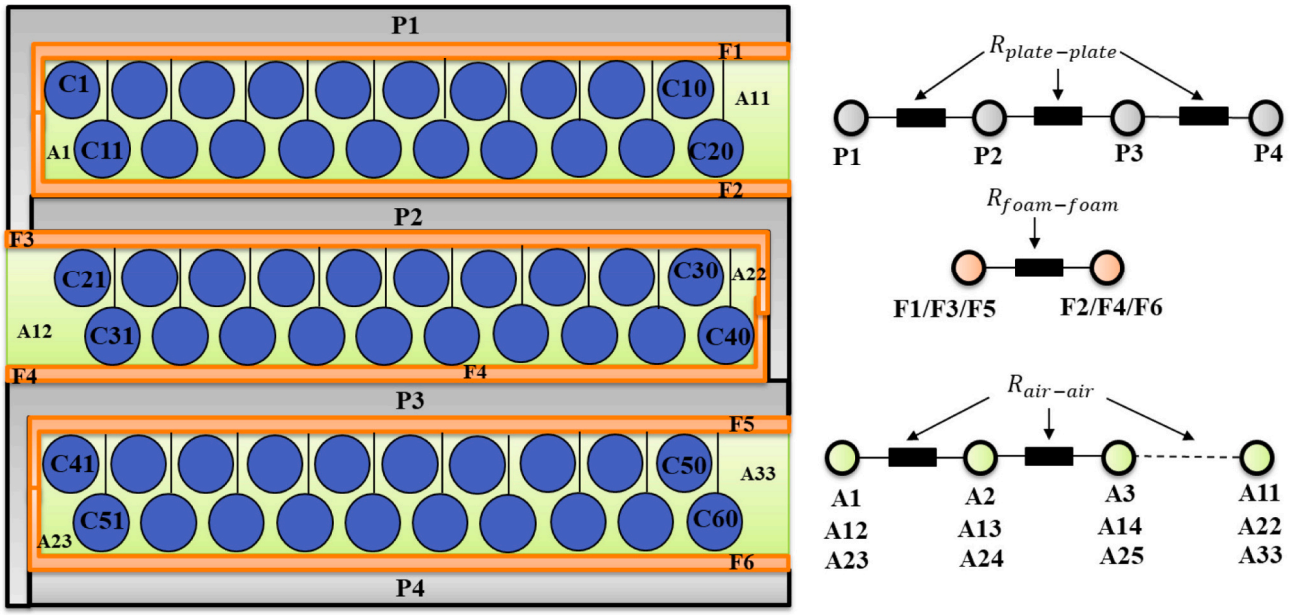

(b)

Fig. 8. Frontal view of the nodal network of the battery module (a) Plane view of the nodal network of the battery module (b).

Table 5
Components of the module and model discretization for the thermal network.

Component	Nodes per unit	Number of components	Nodes in total
Cells	4	60	240
Snake cooling plate	4	1	4
Foam	2	3	6
Water-glycol	5	1	5
Connection tabs	1	13	13
Air	1	33	33
Box	1	1	1
Total	–	–	302

Other thermal resistances, that are not visible in Fig. 8, are considered in the model in order to account for heat transfer between contiguous nodes of the same material/coolant:

- Heat conduction between each air node and contiguous air nodes; a thermal contact resistance is considered for this heat transfer:

$$R_{air-air} = \frac{d_{air\ contiguous\ nodes}}{k_{air} A_{air\ contiguous\ nodes}} \tag{12}$$

- Heat conduction between each foam node and contiguous nodes; again, a thermal contact resistance is considered:

$$R_{foam-foam} = \frac{d_{foam\ contiguous\ nodes}}{k_{foam} A_{foam\ contiguous\ nodes}} \tag{13}$$

- Heat conduction between each cooling plate node and contiguous nodes; again, a thermal contact resistance is considered for this heat transfer:

$$R_{plate-plate} = \frac{d_{plate\ contiguous\ nodes}}{k_{plate} A_{plate\ contiguous\ nodes}} \tag{14}$$

- Heat convection between each coolant node and contiguous nodes; a thermal contact resistance is considered based on the mass flowing through the cooling plate and its specific heat capacity:

$$R_{wg} = \frac{1}{c_{p,wg} \dot{m}_{wg}} \tag{15}$$

- Heat generation is assigned to all electrical connection plate nodes, considering the following expression of the electrical resistance of tab node:

$$R_{el,tab} = \xi \frac{th_{tab}}{A_{tab}} \tag{16}$$

- Specific heat capacity and density values are assigned to each node, in order to calculate their thermal capacitance.

4. Characterization campaign

In order to validate the models, it is needed to characterize the parameters introduced in Section 3. In this section, a detailed analysis of characterization campaign of the electrical parameters is explained, and the main results are shown; the numerical estimation of thermal parameters follows; finally, the experimental characterization of the cooling plate and the estimation of heat transfer coefficient through computational fluid dynamics simulations is provided.

4.1. Experimental characterization of electrical parameters

The electrical parameters of the lithium-ion cell which are needed to be characterized are the following ones:

- Actual capacity of the cell, which varies with respect of temperature and current.
- Open Circuit Voltage of the cell, which varies with state of charge and temperature.
- Resistive and capacitive parameters, which are estimated through post-processing of HPPC test results, and they vary with respect of temperature, charge/discharge rate and state of charge of the cell.

4.1.1. Capacity characterization

To characterize the capacity of the cell in different conditions of discharge rate and temperature, a capacity test is repeated at 3 temperatures (0, 10 and 20 °C) and 6 discharge rates (C/40, C/4, C/2, 1C, 2C and 4C). This characterization allows to have a good estimation of this parameter and of the *SOC*, which depends on the actual capacity from the coulomb counting method. The capacity test consists of a charge of the cell according to constant current – constant voltage protocol (CCCV) [33]. This protocol consists in charging the cell until it reaches the maximum voltage (constant current phase), and then, keeping the voltage constant (constant voltage) and letting the current decrease until it reaches a cut-off value (generally the 5 % of the charge current). After that, the cell is allowed to rest for 1 h, in order to finish all the relaxation process and finally the cell is discharged at constant current until it reaches the allowed minimum voltage.

The results of the characterization of the capacity of the examined cell are shown in Fig. 9.

The capacity of a lithium-ion cell increases with respect of the temperature. This is due to the fact that all the diffusion and mass transport phenomena happening inside the cell are favored at higher temperatures [34]. Furthermore, considering that the nominal capacity of the cell is measured at standard temperature (23 °C) and at 1C, the results obtained at 20 °C can be assumed as a confirmation of manufacturer specification. This aspect can be also expressed as shown in Table 6: for each temperature, the average of the measurements is expressed as a percentage of the nominal value. As expected at 0 °C, the average measured capacity is 9 % less than the nominal value; at 20 °C, instead, the average measured capacity is almost equal to nominal capacity. Furthermore, at a given temperature, it is shown the difference between the maximum and minimum values obtained at different discharge rates. At 0 °C, the discharge rate can't be neglected: discharging the cell at different c-rates leads to a maximum measured difference of almost the 9 % of the nominal capacity; instead, at 20 °C, among the considered discharging rates, it is noticed a much less influence than at lower temperatures [35].

4.1.2. OCV characterization

The OCV has been determined according to quasi-static OCV test protocol: this test is based on a charge and discharge of the cell at a very low current [36]. The test is called "quasi-static" because even though the current is not equal to zero and the polarization processes are not completely absent, it can be considered that all the polarization phenomena neglectable and the terminal voltage can be considered as the ideal voltage provided by the cell when no load is applied, that is the definition of the open circuit voltage [37]. The test carried on in this experimental campaign is composed by a charge of the cell according to the abovementioned CCCV protocol. Then, the cell is discharge at a very low discharge rate, C/40; after that the cell rests 1 h and then it charges at C/40. The quasi-static test protocol is shown in Fig. 10.

The test has been repeated at 3 temperatures in order to analyze possible thermal effect of the OCV measurement, as shown in Fig. 11.

From the test results (Fig. 11), it is evident that the temperature has no relevant effect on the measurement of the OCV. This is hugely documented in literature: temperature effect is known to be more evident only for very low charging level of the battery ($SOC \leq 0.15$). The

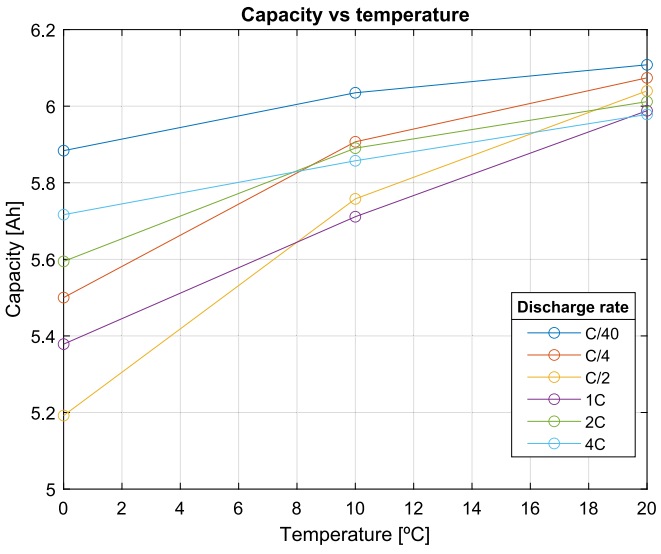

Fig. 9. Capacity test results under different temperatures and discharge rates.

Table 6
Capacity characterization stability analysis.

Parameter under analysis	0 °C	10 °C	20 °C
$\left(\frac{C_T}{C_n}\right) \bullet 100$	91.3 %	97.1 %	100.3 %
$\left(\frac{C_T^{MAX} - C_T^{MIN}}{C_n}\right) \bullet 100$	8.7 %	3.3 %	1.6 %

dependency on the state of charge is much more relevant so that, in the lumped electro-thermal model developed in this work, an average with respect of the temperature is given as an input to the model and the OCV is extrapolated only as a function of the state of charge [38].

4.1.3. Resistive and capacitive parameters characterization

An HPPC test campaign is realized in order to identify resistive and capacitive parameters of the lithium-ion cell under exam. The HPPC test is a very versatile protocol which is adapted to the analyzed cell [39]: in this case charge and discharge pulses are chosen according to the cell charge/discharge rate capabilities. According to manufacturer datasheet, this cell can be discharged and charge up to 4C, and for this reason, the pulses are at maximum as equal as 4C. To identify parameters at different state of charge conditions the cell is initially charge up to 100 % according to CCCV protocol and let rest for 1 h. After that, the cell periodically undergoes the following steps:

1. Cell is discharged of at 10 % at 1C.
2. Cell rests for 1 h to be completely stabilized from a thermal and electrical point of view.
3. Cell undergoes a series of pulses in charge and discharge at C/4, 4C/5, 6C/5, 2C and 4C.

This sequence of steps is repeated until the cell reaches the 10 %. Of course, no pulses sequences are considered in the conditions of fully recharged and fully discharge cell in order not to let the cell operate in over discharge/overcharge conditions.

The test is repeated at 4 temperatures (0, 10, 20 and 40 °C) to have a full comprehension of battery behavior in a wide range of temperatures. The current profile and voltage response of an HPPC test and the zoom of the pulses sequence are shown in Fig. 12.

With the current and voltage profiles, finally, it is possible to obtain resistive and capacitive parameters through an optimization algorithm. First, the ohmic resistance is estimated as the immediate voltage drop (Fig. 13) divided by the pulse current as follows [40]:

$$R_0 = \frac{v_0 - v_1}{I_0 - I_1} \tag{17}$$

Then, the charge-transfer resistance R_1 and the double layer capacitance C_1 are obtained by minimizing the error between the voltage drop measured during the pulse and the regression model optimized in the following equations:

$$err = v_{meas}(t) - v(t) = v_{meas}(t) - (OCV - R_0 \bullet I(t) - v_c(t)) \tag{18}$$

$$v_c(t) = v_c(t-1) \bullet exp\left(-\frac{\Delta t_{1-2}}{R_1 \bullet C_1}\right) + R_1 \bullet I(t-1)\left(1 - exp\left(-\frac{\Delta t_{1-2}}{R_1 \bullet C_1}\right)\right) \tag{19}$$

This means that the RC-branch parameters are optimized in order to reduce error between the model fitting the data for each pulse. This optimization process allows to estimate the resistive and capacitive parameters in all the different conditions considered in the test protocol. The parameters obtained are plotted in Fig. 14 with respect of the temperature.

The analysis of the resistive parameters with respect of temperature shows that, within the range of temperature guaranteed by the manufacturer, the resistances (Figs. 14, 15, 17, 18) decrease with respect of temperature: this is due to the fact that all the losses due to the migration of ions from solid phase to liquid phase are lower at higher temperature due to higher diffusion and mass transport parameters. This Arrhenius behavior noticed in the resistive parameters allows to use a more precise extrapolation model in order to estimate electrical parameters at temperature other than the ones at which the measurements have been done [41]. This allows to greatly reduce test matrix, keeping a good estimation of electrical parameters within the operability window of the cell. From the results, as much as the cell get closer to the fully discharged condition ($SOC = 0$), the resistance increases. On the other side, the double-layer capacitance (Figs. 16, 19) shows an increasing behavior

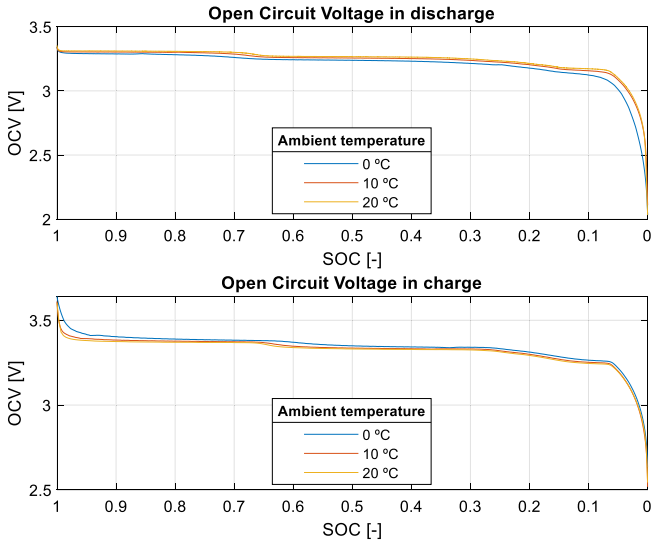

Fig. 11. Quasi-static OCV test results.

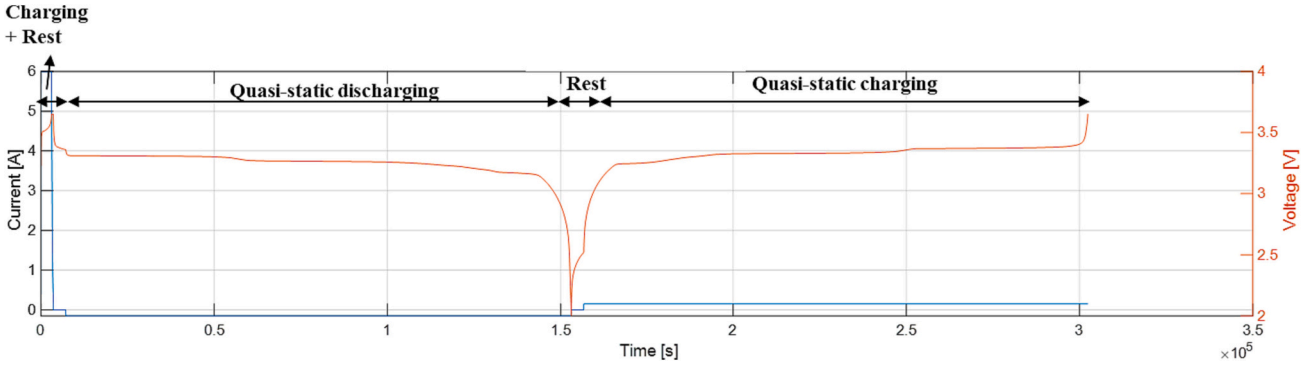

Fig. 10. Quasi-static OCV test protocol.

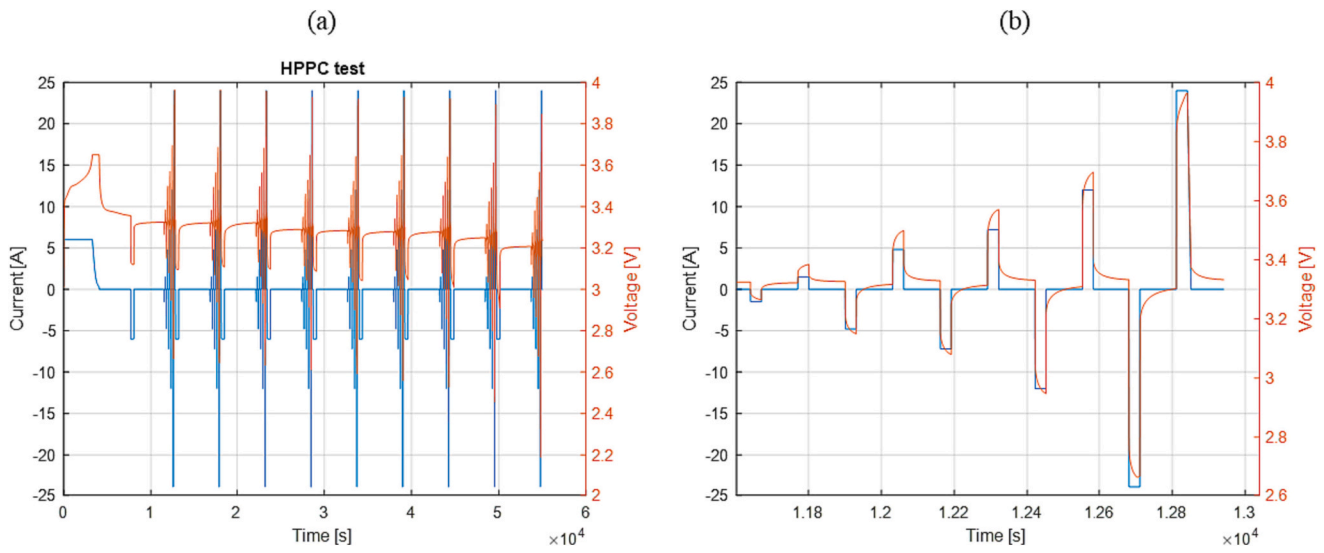

Fig. 12. HPPC test profile (a); Charge/discharge pulses sequence (b).

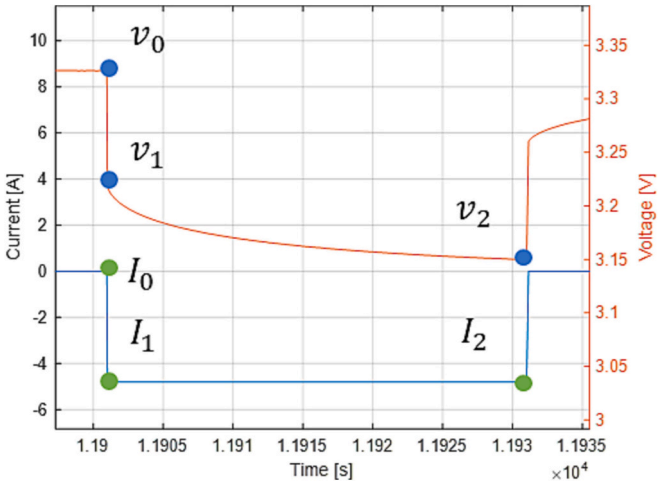

Fig. 13. Pulse method for parameters identification.

with respect of the temperature and as much as the cell get closer to fully charged condition ($SOC = 1$), the double-layer capacitance increases.

4.2. Numerical estimation of thermal parameters

The following thermal parameters of a lithium-ion cell need to be calibrated:

Thermal capacity of the lithium-ion cell $C_{th} = \rho c V$.

- Thermal conductivity along radial direction k_r
- Thermal conductivity along axial direction k_a.

In this work, these parameters have been determined fitting experimental data [42]. Simulations have been iterated until the error between model output and experimental measurement has been minimized. The abovementioned parameters have been optimized at 1C charge (Fig. 15a), and then the model agreement with experimental data has been evaluated in the other conditions discharge rates at 1C, 2C and 4C as Fig. 15 shows.

The values obtained from model fitting are $C_{th} = 180 \frac{J}{K}$, $k_r = 0,2 \frac{W}{mK}$, $k_a = 32 \frac{W}{mK}$.

The RMS errors of the model fitting the experimental data in the 4 different cases are shown in Table 7.

From Table 6 and considering the huge available literature about usual thermal capacity and thermal conductivities [43] values of a lithium-ion cell, it can be concluded that the values obtained from the optimization process are precise enough to describe thermal behavior of the lithium-ion cell [44].

4.3. Experimental characterization of the cooling plate

To accurately estimate the pressure loss in the cooling plate, an experimental test bench for its characterization has been designed and constructed (description in Section 2). The cooling plate has been tested at constant temperature ($25°C$). The results of the characterization campaign are shown in Fig. 16.

Each measurement consists in the following steps:

- Manual regulation of the volumetric flow.
- 30 s measurement at the maximum frequency allowed by the data-logger ($f_{meas} < 1\ Hz$).
- Average of the measurement and obtention of the point on the volumetric flow – pressure drop plot.

First of all, the pressure sensors are calibrated and if necessary, an offset is set in order to begin the measurement with $p_{in} = p_{out}$. Due to pump limitation, it has been possible to measure the curve up to $3 \frac{l}{min}$, the measurements allow to calibrate a regression model to estimate pressure losses at higher volumetric flow than measured [45]. The fitted regression model has the following expression:

$$\Delta p_{mod} = \Delta p_0 + s_p \bullet \dot{V}_f^2 \tag{20}$$

Once determined the optimal values for the offset Δp_0 and the coefficient s_p, a coefficient of determination $R^2 \cong 97\%$ is obtained. Finally, the Sieder and Tate correlation [46] has been used for heat transfer coefficient calculation (Eq. (21)) and the results are shown in Fig. 17 for 4 different volumetric flows.

$$\mathrm{Nu} = \left[\left(\frac{\mathrm{D}}{\mathrm{L}}\right) Re\ Pr\right]^{0,33} \left(\frac{\mu}{\mu_s}\right)^{0,14} \tag{21}$$

5. Validation of the cell electro-thermal model

The model has been validated experimentally with a normalized real driving emission cycle. From the required power, the current profile has

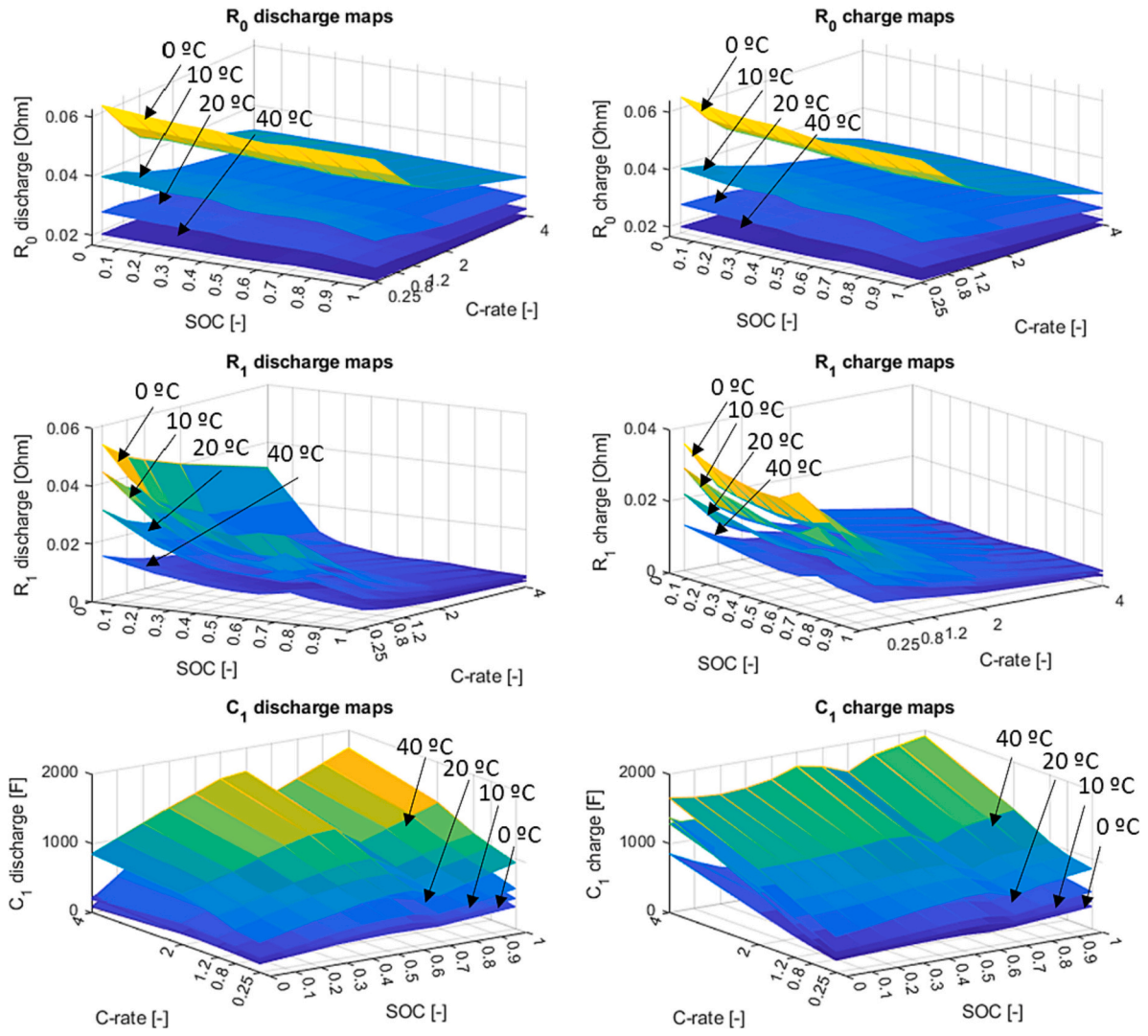

Fig. 14. Electric parameters maps.

been obtained and it has been integrated in the battery cycler (Fig. 18).

The current profile has been expressed in terms of c-rate: this validation allows to validate the battery electric behavior in multiple c-rate conditions, making the validation process more general and valuable than a single rate charge/discharge validation cycle. Current and voltage are measured, and the experimental voltage has been compared to the modeled voltage. The test has been carried out at 23 °C. Three thermocouples have been placed on the cell surface to measure temperature: two thermocouples are placed on the terminals of the cell and a third thermocouple is placed on the center of the lateral cylindrical surface. The agreement of the model results has been evaluated according to the root mean square error indicator:

$$\mathrm{rmse}_{\%} = \frac{\sqrt{\frac{1}{n_1}\sum_{i=1}^{n_1}\left(v_{sim} - v_{meas}\right)^2}}{\mathrm{mean}\left(v_{meas}\right)} \bullet 100 \tag{22}$$

The results of model agreement are shown in Figs. 19-20.

The errors for the electrical model and the thermal model are summarized in Table 8.

In order to further validate the model and considering the application of the module for an e-bus, another cycle has been considered. A route of a touristic electrified bus has been used to analyze discharge capability of the cell. The normalized current and voltage profile are provided in Fig. 21 for a particular route. Furthermore, the bus is supposed to start from a fully charged condition ($SOC = 1$) and to finish the cycle at about $SOC = 0.3$.

The characteristics of the bus are summarized in Table 9.

With the information provided for the bus battery and the cycle represented in Fig. 26, it is possible to obtain a normalized current profile for the 32,700 cell under exam. In order to get a correct estimation of the current profile, the power required to the bus must be provided by a theoretical battery pack composed by the 32,700 cell:

$$P_{batt.bus} = V_{batt.bus} \bullet I_{batt.bus} = v_{cell} \bullet I_{cell} \bullet N_{cell.total} \tag{23}$$

Once calculated the number of cells in parallel and in series, keeping the power and energy requirements,

$$\mathrm{N_{cell.series}} = \frac{\mathrm{v_{n.batt}}}{\mathrm{v_{n.cell}}} \tag{24}$$

$$\mathrm{N_{cell.parallel}} = \frac{\mathrm{C_{n.batt}}}{\mathrm{C_{n.cell}}} \tag{25}$$

and considering that:

$$N_{cell.total} = N_{cell.series} \bullet N_{cell.parallel} \tag{26}$$

it is possible to estimate the correct current profile for the 32,700 cylindrical cells under exam.

The current profile has been implemented in the battery cycler

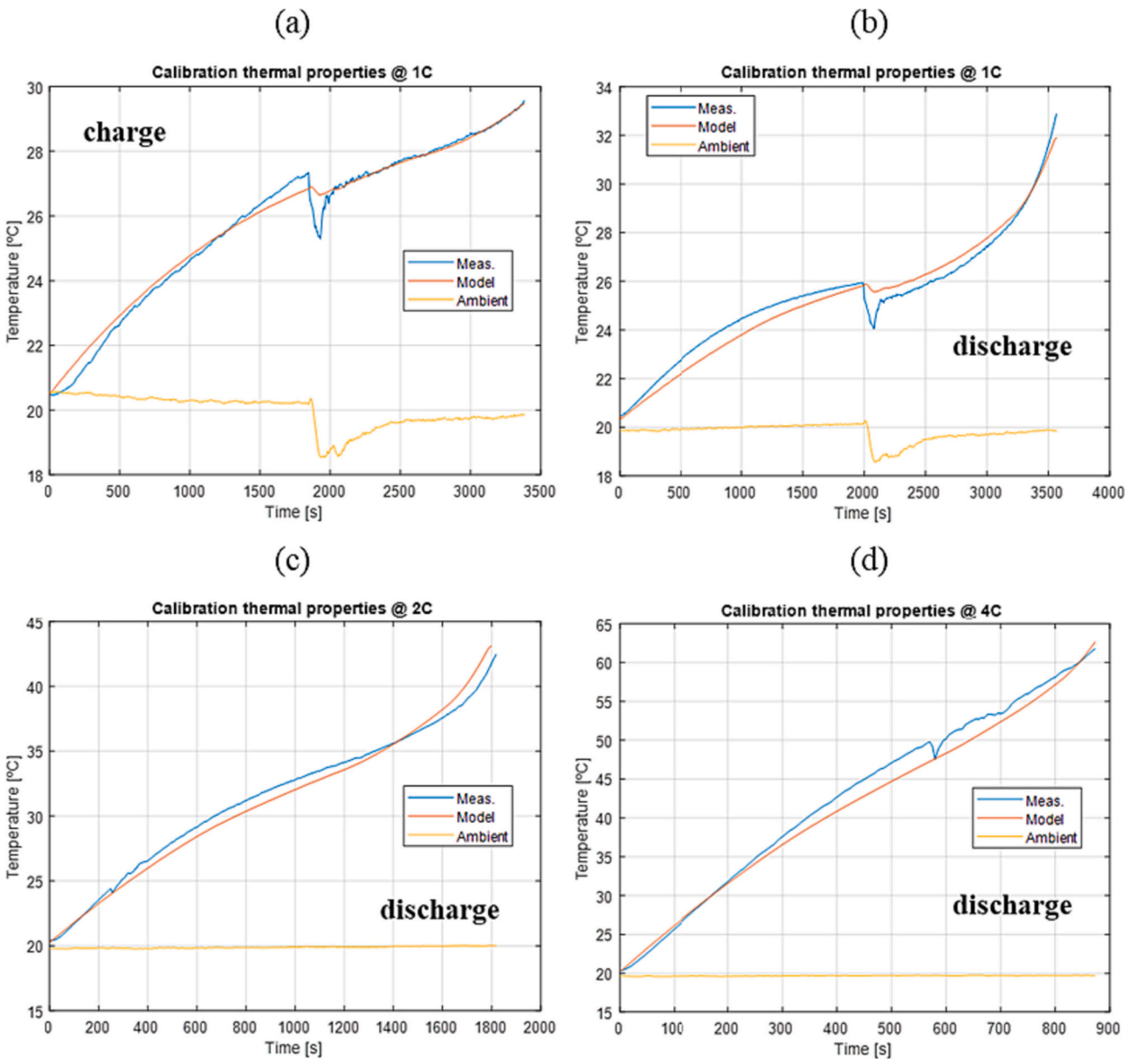

Fig. 15. Calibration of thermal parameters in the 4 different conditions.

software and the cell has been cycled at 2 temperatures, 0 and 20 °C. The results are given in terms of measured and modeled state of charge in Fig. 22. The model can accurately describe the discharge capability of the cell, enlightening the differences according to cell power requirement and temperature of the test. The following expressions have been considered, respectively, for the measured and modeled state of charge:

$$SOC_{meas} = SOC_0 - \frac{\int_{t_0}^{t_f} v_{meas}(t) \bullet I(t)dt}{3600 \bullet C_{Ah}} \tag{27}$$

$$SOC_{sim} = SOC_0 - \frac{\int_{t_0}^{t_f} v_{sim}(t) \bullet I(t)dt}{3600 \bullet C_{Ah}} \tag{28}$$

From the results it can be understood that lower temperatures lead to higher energy discharge for the bus battery. This can be particularly interesting when the bus is operating in a very harsh climate condition or in a milder one: in fact, the battery at 0 °C discharges about 6 % more than at 20 °C [47]. Using the model, it is possible to estimate the further battery cell discharge at very low temperature. In Fig. 23, it is possible to observe that in a bus cycle at −20 °C, 15 % higher discharge than at standard temperature is produced in the cell. This indicates that at these very low temperatures, very likely the battery could be almost totally discharged at the end of the cycle. For this reason, the development of a good thermal management system is fundamental to let the battery operate always in the optimal temperature range. The reason of this further discharge is due by the fact that at lower temperatures two negative phenomena are having impact on cell performance. From one side the capacity of the cell decreases leading to a quicker discharge of the cell. On the other side the resistive parameters of the cells increase, and consequently heat losses increase.

6. Thermal analysis

By using the developed numerical tools, it is possible to analyze the module from a thermal and energetical point of view [48]. The case study is the charging process of a battery module at different charging rates. The charging process is considered to start at $SOC = 0$ and to finish at $SOC = 1$. This analysis has very important outcomes [49]:

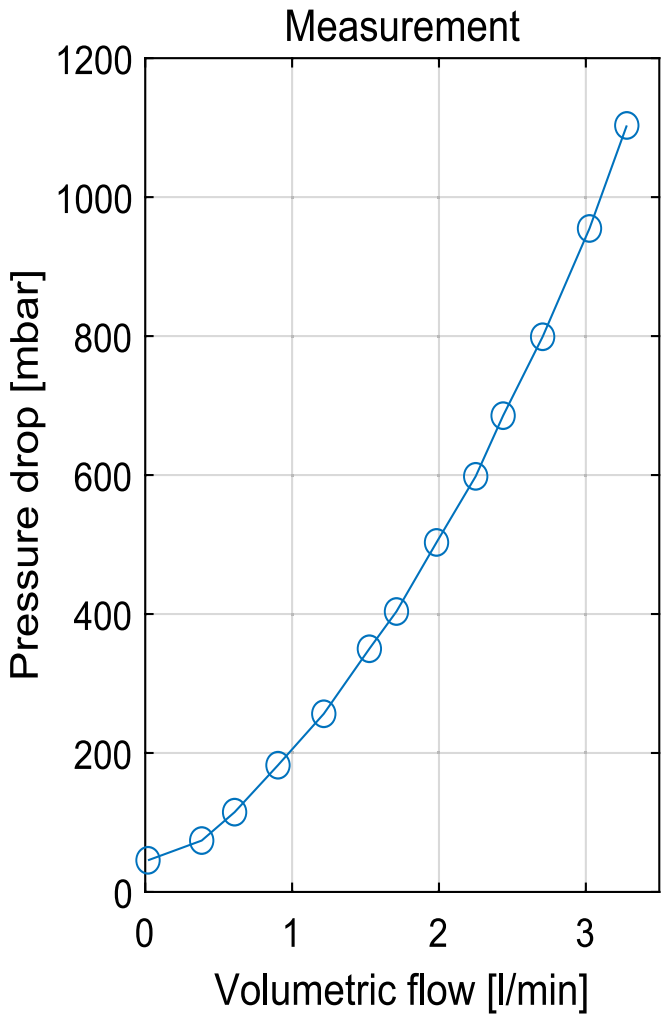

Fig. 16. Pressure drop measurements.

Table 7
RMS errors for thermal parameters estimation through numerical fitting.

	1C charge	1C discharge	2C discharge	4C discharge
RMSE [°C]	0.28	0.48	0.70	1.46

- It allows to design adequately a thermal management system according to environment conditions (ambient temperature) and heat generated by the module (which depends on the rate of charge).
- It allows to find the hot spots of the module which can eventually be the trigger of a thermal runaway of the entire module.
- It allows to evaluate the performance of the module coupled to the serpentine cooling plate operating at any demanded condition.

The thermal analysis of the module is assessed by quantifying the impact that the variation of 4 operation parameters ($T_{amb}, c_{rate}, T_c, \dot{V}_f$) has to the following 3 variables:

- Peak temperature in the module at the end of the charging process, T_{max}.
- Thermal gradient between the cells of the module at the end of the charging process, ΔT_{cells}.
- The time interval that the cells spend within the optimal temperature range $[15\ 35]^{\circ}C$ over the total charging time, $(\Delta t_{opt}/\Delta t_{chg})$.

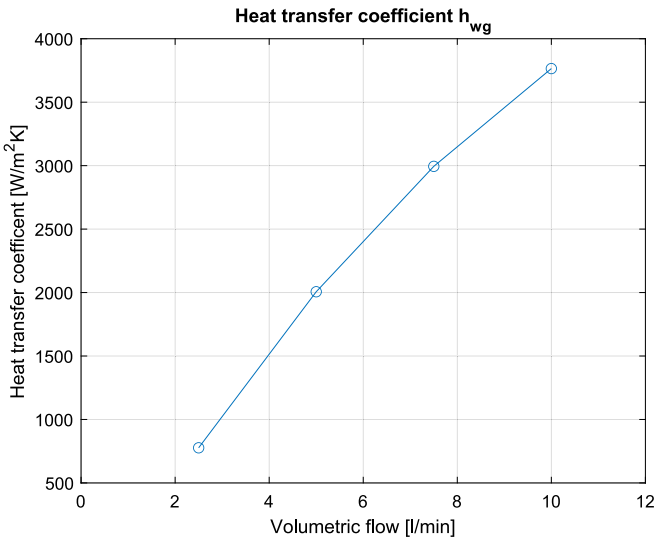

Fig. 17. Estimated heat transfer coefficient.

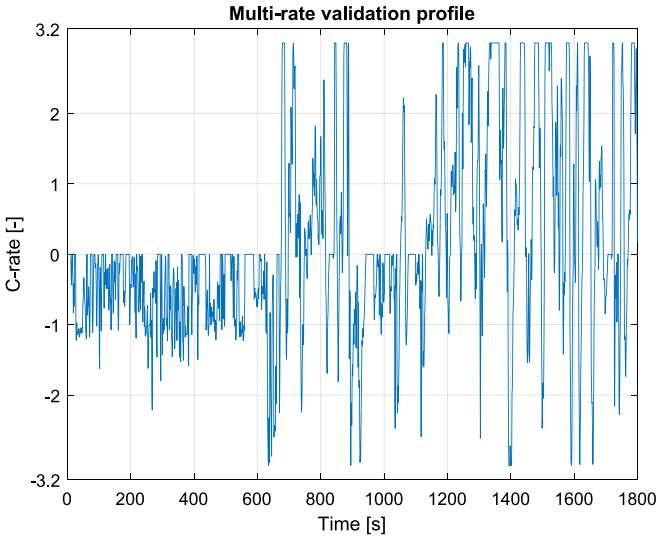

Fig. 18. Multi-rate profile for model validation.

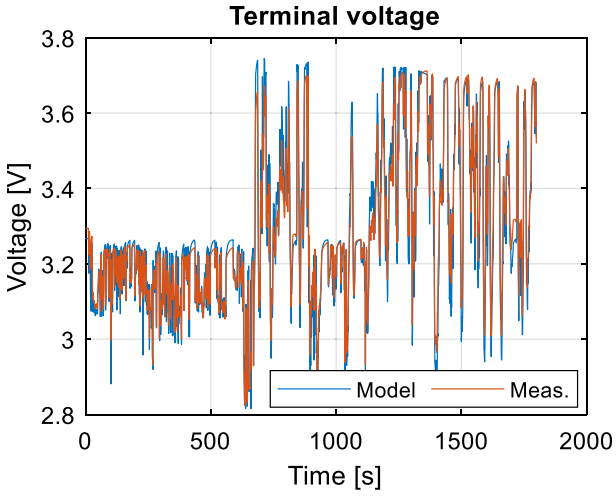

Fig. 19. Validation of the electrical model.

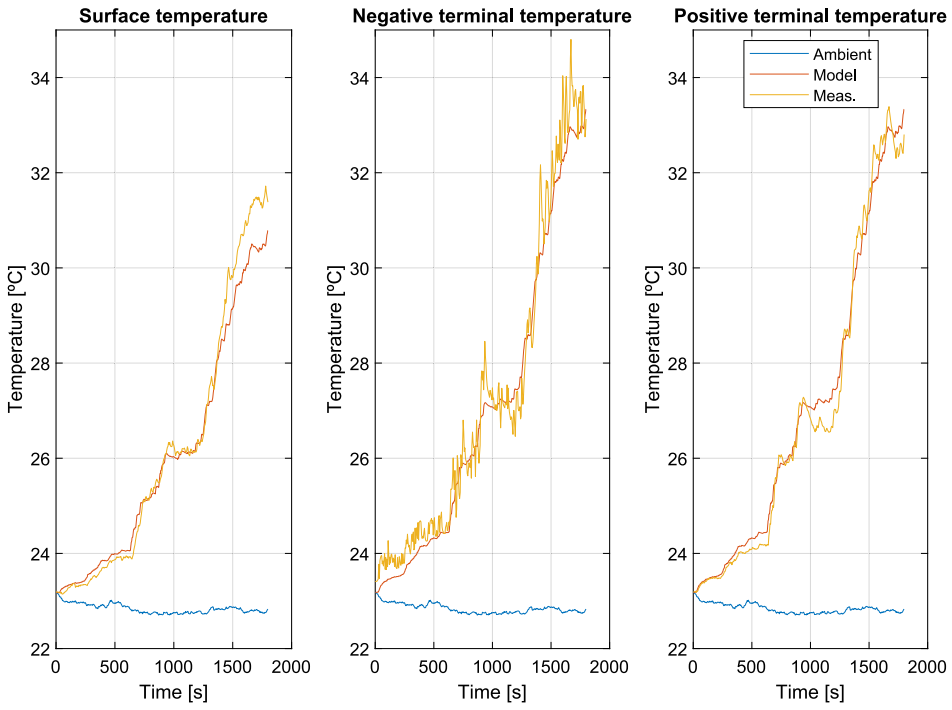

Fig. 20. Validation of the thermal model in the lateral surface (a), in the negative terminal (b), in the positive terminal (c).

Table 8
Root Mean Square Errors for the model.

Variable	RMSE [%]
Terminal voltage	1.44
Surface temperature	1.95
Positive terminal temperature	1.20
Negative terminal temperature	1.90

Table 9
Bus characteristics.

Characteristic	Value
Battery capacity [kWh]	150
Battery nominal voltage [V]	616
Number of cells in series	168
Number of cells in parallel	1

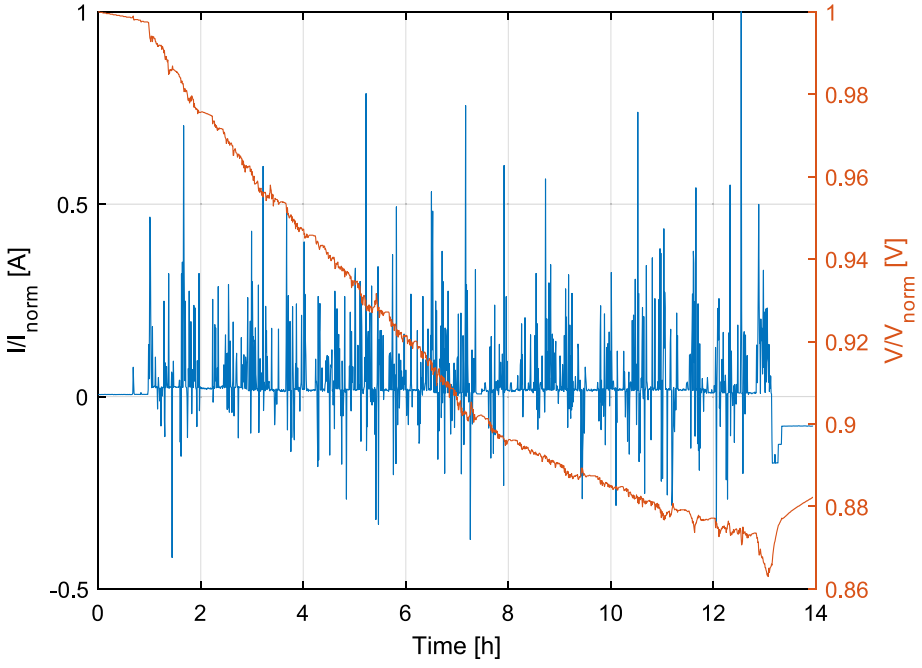

Fig. 21. Normalized current and voltage profiles for a touristic bus route.

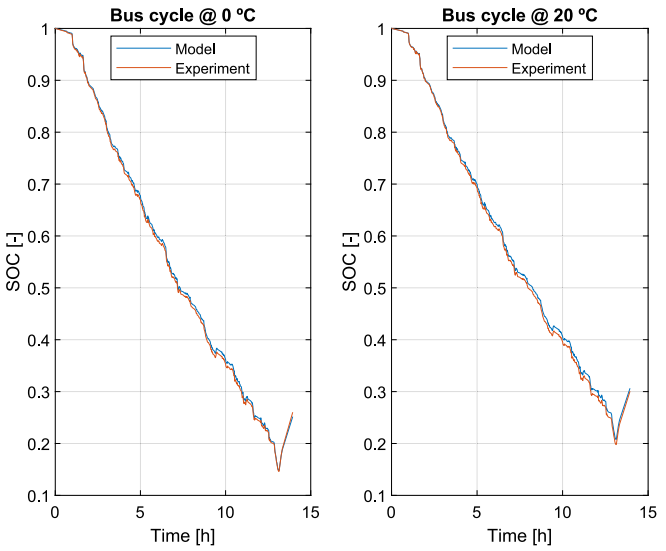

Fig. 22. Agreement of the model in terms of SOC evolution at 0 and 20 °C.

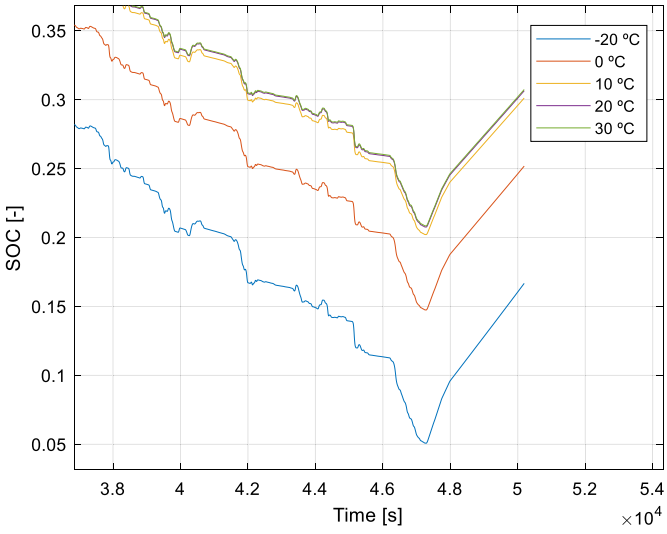

Fig. 23. Estimated discharge of the battery cell at different ambient temperatures.

With this aim a parametric study that required 240 simulations have been carried on. The 4 parameters have varied within reasonable ranges as follows:

- Charge rate: 1C, 2C, 3C and 4C.
- Ambient temperature: 0, 10, 20, 30 and 40 °C.
- Coolant temperature: 10, 20 and 30 °C.
- Volumetric flow: 2.5, 5, 7.5 and 10 l/min.

Results of the thermal analysis are shown in Figs. 24 and 25for two scenarios: hot climate conditions (T_{amb} = 40 °C) and cold climate conditions (T_{amb} = 0 °C). The rows shown in each figure correspond to the contour plots of the 3 variables obtained with each C-rate considered in the study. The coolant temperature is supposed to vary between 10 and 30 °C. This situation would be the case in which the coolant is interacting with the A/C circuit, since otherwise the coolant would be at the same temperature as the environment. On the other hand, it is not a goal of this study to go further in showing how a possible A/C circuit for coolant refrigeration works. In this case, it will be supposed that the A/C circuit provides the coolant at a given temperature and it will be analyzed its impact on the cells' thermal evolution. The goal of this analysis is to find out the volumetric flow and coolant temperature (operation point of the cooling system) which allow to charge the battery module keeping is temperature below the temperature limit indicated by the manufacturer. For this cell, the temperature limit indicated by the manufacturer is 45°C.

In the hot climate condition case (T_{amb} = 40 °C), at the beginning of the charging process, the cells are at a temperature higher than the temperature of the coolant. Hence, the coolant is surely cooling down the cells of the module. Looking at the maximum cell temperature in the module, independently of the coolant temperature, the increase of its volumetric flow leads to lower cell temperatures. On the other hand, at the same volumetric flow, the coolant temperature decrease will reduce the cell temperature in the module. Regarding the spatial temperature difference, the trends are the opposite to that observed for the maximum cell temperature. The temperature gradient is reduced as the volumetric flow of coolant increases and as the coolant temperature increases. Fig. 24 also shows that the cells operate more time in the optimal temperature range as the volumetric flow increases and the temperature decreases [50].

In the 1C charging process, the temperature is kept below the temperature limit for each operation point considered in this analysis. Of course, increasing the volumetric flow and decreasing the coolant working temperature, the maximum temperature in the module can be kept around 20–25°C, which is the optimal thermal operation point for lithium-ion cells. Furthermore, the thermal gradient in the module can be kept below 1 °C for the highest volumetric flow considered in this analysis and the time spent within the optimal temperature range can be up to 85 %. From the user point of view, of course, it is interesting to reduce as more as possible the duration of the charging process. Nowadays, the automotive manufacturers have pushed the duration of the charging process down to 20 min. If it is considered a complete charging process from $SOC = 0$ to $SOC = 1$, this means to charge the battery at 3C. Looking at Fig. 24, it can be observed that only a limited portion of the cooling system operation points can satisfy the condition of $T < 45°C$: in particular only for volumetric flows above 3 l/min and coolant temperature below 18 °C, this condition is satisfied.

The situation radically worsens going to the 4C charging process: this ambitious milestone has not been achieved yet and with the cooling system designed for this battery module, the temperature in the module achieves critical values and the battery module spends most of the charging process duration outside the optimal temperature range.

In the cold climate condition case (T_{amb} = 0 °C), at the beginning of the considered charging velocities, the coolant should heat up the cells because such low temperature could accelerate all the ageing mechanisms inside the cells such as formation of dendrites and loss of lithium inventory and capacity loss. All the previous observations about coolant volumetric flow and temperature impact to maximum cell temperature and gradient apply as well. However, the monotonic trend of the cell operating time in the optimal temperature range observed at warm ambient conditions does not happen. At 4C charging battery cells operate at optimum temperature range longer time than during 2C and 3C rates. In this case, the self-heating of the cells aid the thermal management system to achieve the optimal temperature range quicker.

Regarding the 1C charging, it is observed that all the possible operation points considered in this analysis keep the battery temperature within a reasonable operation temperature range: the highest temperature achieved is 32 °C, considering the coolant working at 30 °C. On the other hand, the lowest temperature is achieved in the case the coolant temperature is equal to 10 °C: in this case the battery module achieves 18 °C. As it is hugely commented and shown in literature, the battery optimal temperature is included between 20 and 25 °C. Therefore, it would be better to operate the cooling system at a higher temperature than 10 °C in this case, to achieve higher working temperatures for the battery module. In this case the time spent within the optimal temperature range can be go up to 80 % of the total charging process duration.

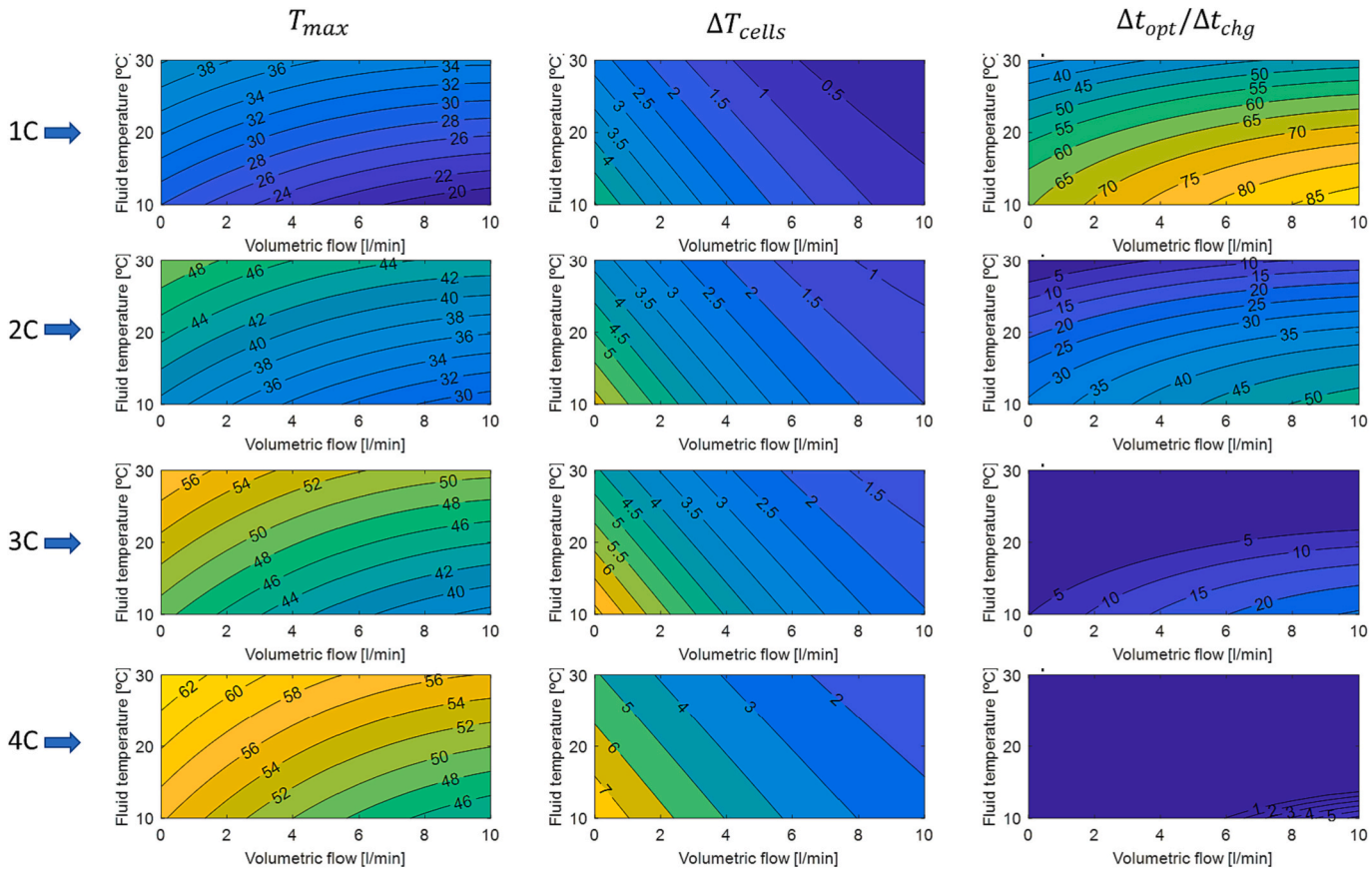

Fig. 24. Results of thermal analysis at 40 °C.

As well as for the hot climate condition case, also in this case the 3C charging process has been taken as a fast-charging process according to current state of technology. In this case the charging process would last only 20 min for a complete battery recharge and the temperature achieved during the process are always below the thermal limit. Compared to the hot climate condition, this case seems to be less critical from the point of view of the maximum temperature achieved in the battery module, because any operation point within the ranges above specified, can satisfy the thermal limitation imposed by the manufacturer. On the other hand, the drawback is that in this case the charging process starts at low temperature, which can shorten the lifespan of the battery due to acceleration of the ageing processes. This ageing aspect is not considered in this work, but it should be analyzed in a deeper analysis of the cooling system design for charging of battery modules. For example, the battery could be pre-heated up to an established initial battery charging temperature and then, the charging process could be started.

Complementary to the thermal analysis, an energetic analysis of the battery module can be done.

This analysis allows to identify the amount of energy which is effectively stored inside the battery and the energy which is lost because of the heat generation. Furthermore, all the heat generated inside the battery module is divided into 2 aliquots: the heat absorbed into the module which causes the increase of the cells temperatures and the heat dissipated into the coolant. The knowledge of the actual heat generation is fundamental to estimate the battery module energy efficiency, while the knowledge of the heat dissipation is used for evaluating the battery cooling system capabilities.

For the abovementioned parametric study, an energy balance of the module during the charging process has been considered. The total energy supplied to the module is expressed by Eq. (32) [51]. Since in every case the charge process finishes when the module achieves the fully charged condition ($SOC = 1$), the energy supplied to the module is the same.

$$E_{supplied} = \sum_{i=1}^{N_{cells}} \int_{t_0}^{t_f} \left(v_{cell,i}(t) \bullet i(t) \right) \bullet dt \tag{32}$$

In this model, the energy supplied to the battery is the sum of two aliquots, which are the electric energy stored in the cells and the heat generated by the cells in the module:

$$E_{supplied} = E_{stored} + Q_g \tag{33}$$

The electric energy stored corresponds to the capacity with which the module has been effectively charged. The rest of the energy supplied to the module has been lost as heat generated by the cells.

This energy balance can be expressed in percentage as show the bar plots of Fig. 26.

The energy balance is presented for 12 different cases which can be divided in 3 scenarios: the first scenario, represented by the 4 plot in the first row, takes into account the case in which $T_{amb} = T_c$, that could represent the charge of the battery after a long stop; the second scenario, represented by the 4 plots in the second row, considers the case in which $T_{amb} < T_c$, that mimics the charge of the battery in a cold climate and with the BMS in heating mode; the last scenario considers the case in which $T_{amb} > T_c$ and it is represented by the plots in the bottom row. This last case could represent the charging of the battery in very warm condition and with the BMS in cooling mode. For each scenario, four coolant volumetric flows are considered in the analysis. Finally, each plot shows the value of the heat generated and the electric energy stored in the cells relative to the total supplied energy for 4 different charging rates.

It can be observed that, regardless of the considered case, the energy stored in the cells is always higher than 90 %. This result could be assumed as a global energy efficiency of the module charging process.

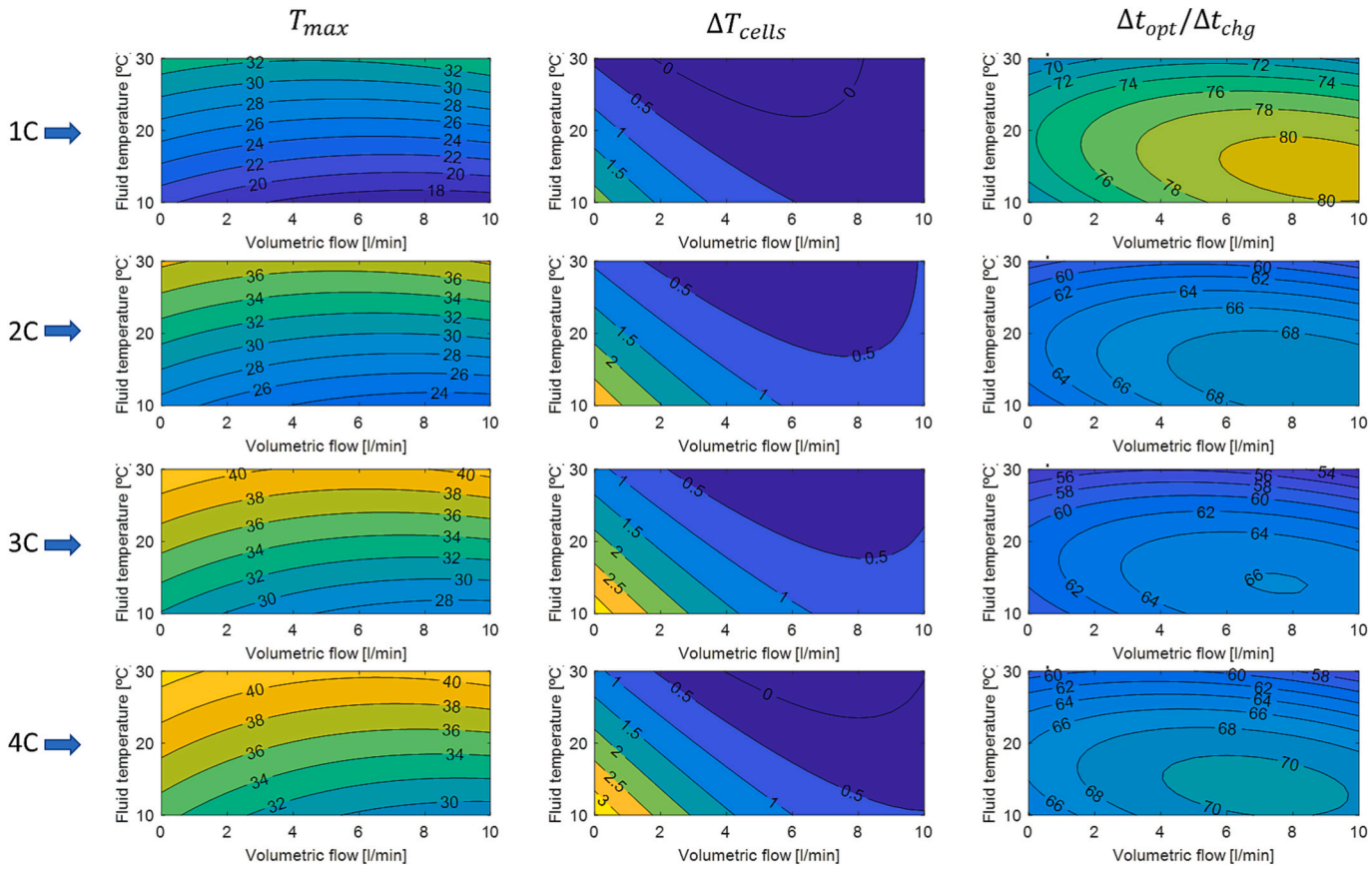

Fig. 25. Results of thermal analysis at 0 °C.

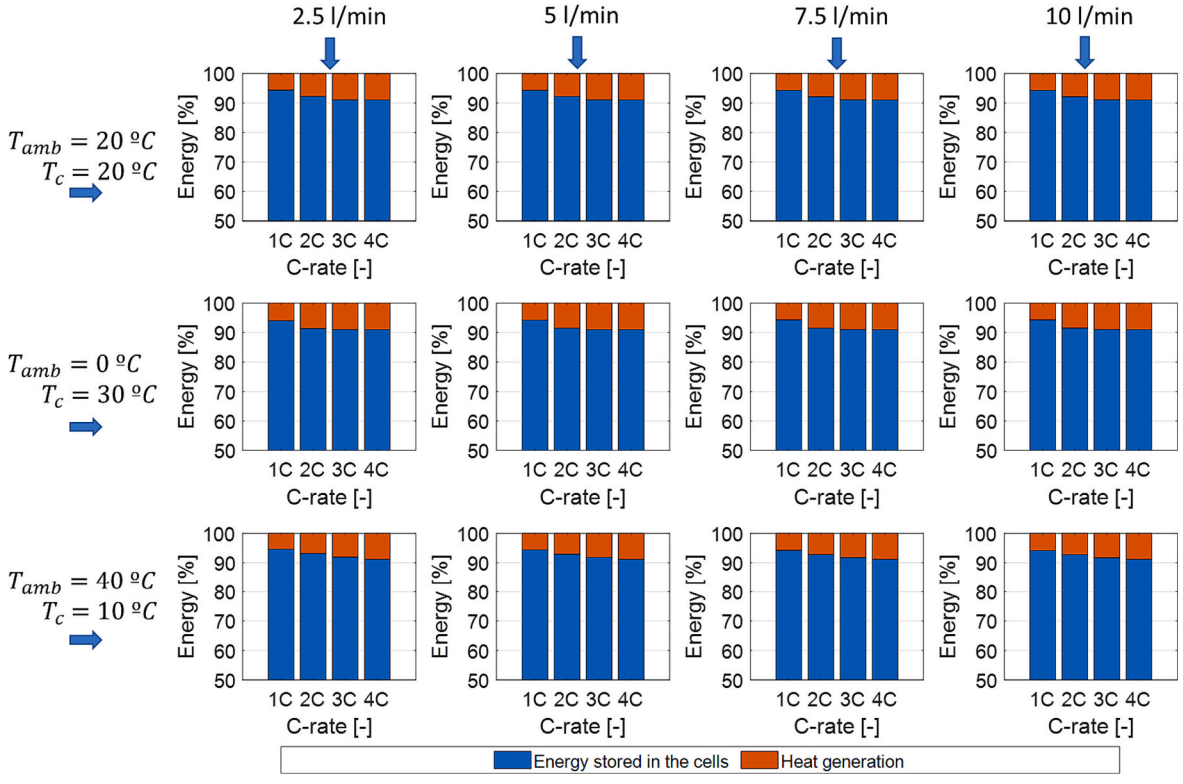

Fig. 26. Bar plot of energy stored and heat generated by the cells in percentage.

Furthermore, the heat generation percentage gets higher as the module is charged at higher charging rate. Besides, results in Fig. 26 show that the effects of coolant flow and temperature are negligible in comparison with the charge rate effect.

The heat generated by the cells, that is inversely proportional to the charging efficiency, strongly depends on c-rate as can be concluded observing every row of Fig. 27.

The generated heat increases exponentially as the charging rate increases for moderate ambient temperatures while it rises almost linearly for extremely warm ambient temperatures. Furthermore, comparing the four plots of every column, it can be checked that the thermal boundary conditions of the module (ambient temperature, fluid temperature and mass flow) have an impact on the heat generation of the cells, but is negligible in comparison with the charge rate effect. The heat generation can also be expressed as the algebraic sum of two terms representing the heat dissipated by the cells to their surroundings (module components, the coolant and air) and the heat absorbed by cells which contributes to increase their temperature.

$$Q_g = Q_{abs} + Q_d \tag{34}$$

The total heat absorbed by cells and the heat dissipated can be expressed by Eqs. (35, 36), respectively:

$$Q_{abs} = \sum_{i=1}^{N_{cells}} \left(T_{cell,end,i} - T_{cell,0,i}\right) \bullet C_{th} \tag{35}$$

$$Q_d = \sum_{i=1}^{N_{cells}} \int_{t_0}^{t_f} \left(T_{cell,i} - T_{surf,i}\right) \bullet k_{core,surf} \bullet dt \tag{36}$$

The heat absorbed in a cell depends on its temperature variation during charging and the thermal capacity of the cell, as it is shown in Fig. 28. Therefore, if the cell temperature increases during charging, this term will be positive, while in the opposite situation the heat absorbed will be negative. A negative absorbed heat represents a heat which is dissipated to the other elements. In the same way, a positive heat dissipated by the cells means that heat is transferred from the cell to the surroundings, and a negative dissipation indicates that heat is transferred to the cell core.

Regarding the results shown in Fig. 28, the following remarks can be done:

- When $T_{amb} = T_c$, both the heat dissipated and the heat absorbed in the cells are positive. This is due because, for each condition analyzed, the cells heat up during charging and their temperature is always higher than those of the other elements.
- When $T_{amb} < T_c$, the cells still heat up during charging in each condition analyzed, therefore the absorbed heat is positive. Nonetheless, in this scenario, the coolant is heating up the module to make it work in a milder range of temperatures. Therefore, the heat dissipated is negative, which means that heat is transferred from the coolant to the cells.
- When $T_{amb} > T_c$, the heat dissipated is obviously always positive, that is cells transfer heat to the other elements in the system. The heat absorbed can be either positive, when the heat dissipated to the surroundings is higher than the heat generated by the cells, as in 1C—2C charging with 2.5 l/min of coolant flow case, or positive when the heat generated by the cells is higher than the heat dissipated from the cells, as in 3C—4C charging with 2.5 l/min of coolant flow case.

Taking advantage of the suitability of the proposed model to evaluate the thermal state of the different components of the module, it is interesting to discern the distribution of the heat between the different components of the module. For this analysis, the scenario with the

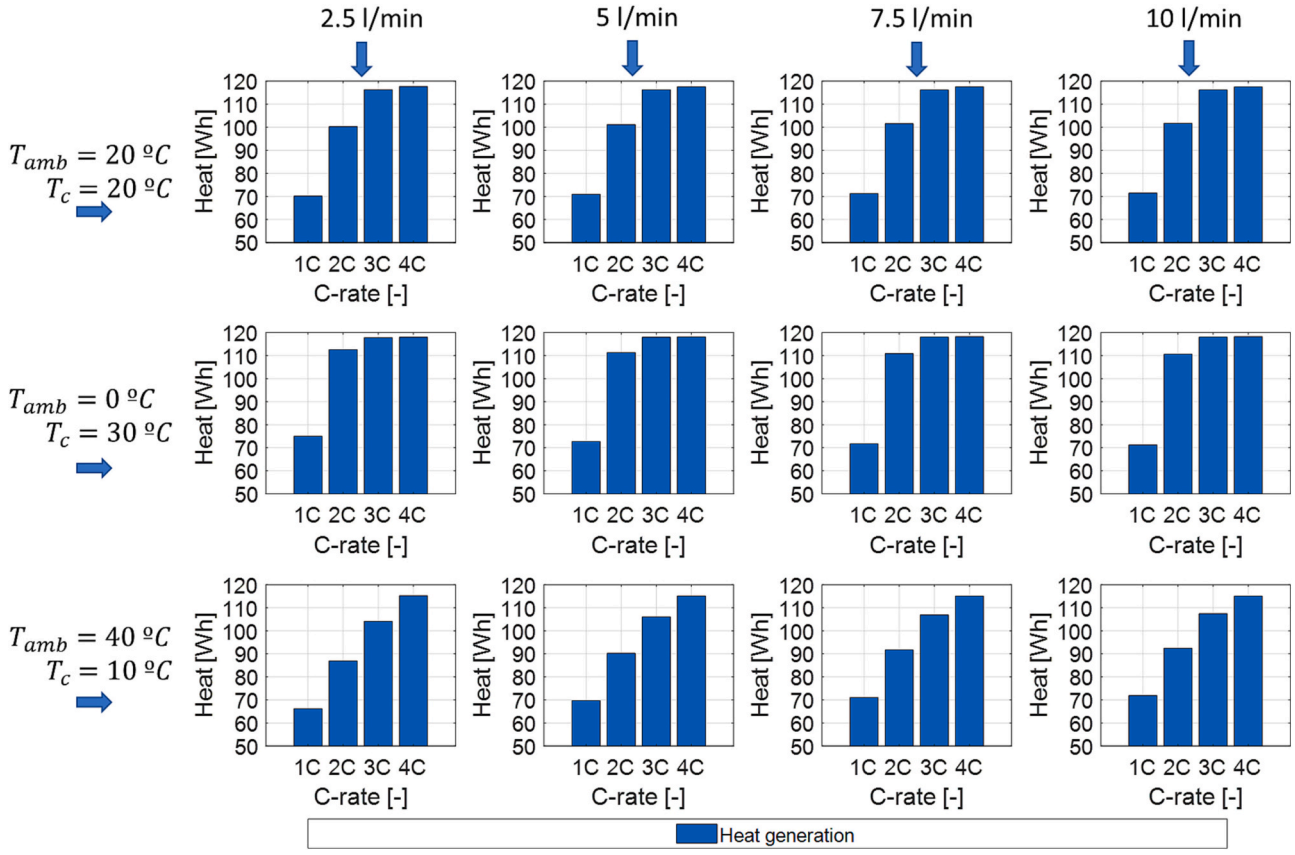

Fig. 27. Bar plot of the heat generation by cells.

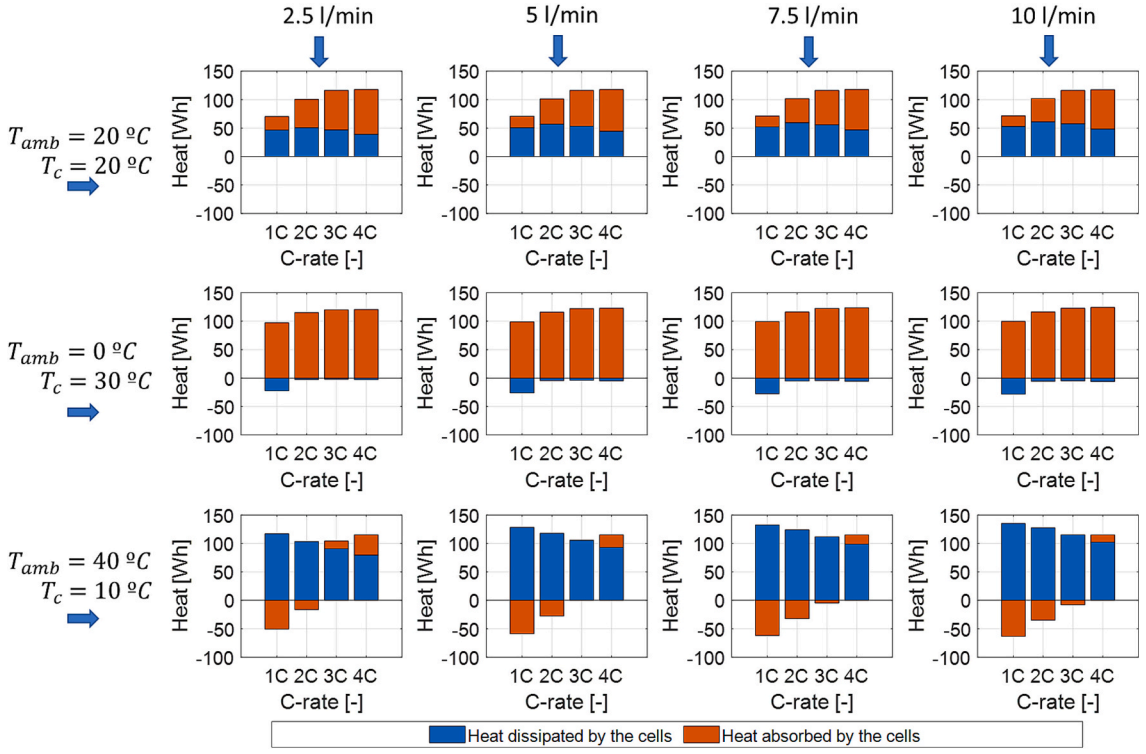

Fig. 28. Bar plot of the heat dissipated by the cells and the heat absorbed in the cells.

warmest ambient (40 °C) and the lowest coolant temperature (10 °C) has been considered. At such conditions the heat dissipated by cells is always positive. Fig. 29 shows pie diagrams of the distribution of the heat transferred from the cells to the coolant and the other module components at different charging velocities (rows) and coolant flows (columns).

As expected, these results show that the heat absorbed by the module components is highly dependent on the charging velocity. At 4C, almost 20 % of the heat dissipated by cells is absorbed by these elements, confirming the possibility of creating undesirable hot spots in the module. The results also show the small dependance of coolant heat dissipation on the coolant volumetric flow, which produce a scarce increase of 2 % of the heat dissipated by cells at maximum flow increase.

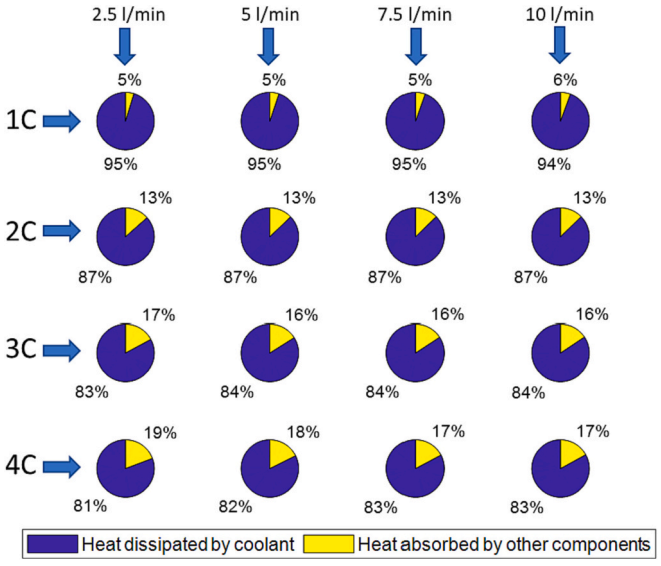

Fig. 29. Distribution of the heat transferred from the cells to the coolant and the other module components at different charging velocities and coolant flows.

7. Conclusions

In this work, a lumped model of a lithium-ion battery module composed by 32,700 cylindrical cells cooled by a serpentine cooling plate is presented and validated. The suitability of the model to assess thermal issues in vehicle batteries is also shown. The results of this investigation lead to the following conclusions:

- The model has been validated against measured data in a high-dynamic driving cycle showing a good agreement both for the electrical variables (terminal voltage and state of charge prediction) and the thermal parameters (temperatures of terminals and surface). The RMS errors of the thermal part are all less than 2 %.
- An electric bus route has been used to confirm the reliability of the model to identify the impact of temperature operation to the performance of the module. The bus route simulation predicted an over discharge of the module of 6 % when it operates at 0 °C rather than at 20 °C. This observation confirms that, due to resistances increase and capacity loss, the cells of the module discharge quicker as the operation temperature decreases.
- The cell peak temperature in the module, the cell temperature gradient and the time spent by the cells within the optimal temperature range were the parameters considered in this investigation to characterize the thermal state of the module at different charging rates (from 1C to 4C) and thermal boundaries. Results obtained for the most critical situation (warm climate module operation) show that at ultra-fast charging rate (3C) the cooling system allows to keep the operation temperature of cells within the optimal temperature range <4 min ($\frac{\Delta t_{opt}}{\Delta t_{chg}} < 20\%$). However, the peak temperature at the end of charging does not reach the maximum operating temperature specified by the cell manufacturer (45 °C) and the temperature gradient is maintained below 2.5 °C, which is acceptable for battery operation.

- The energy analysis of the set of cells in the module during charging has shown that independently of the thermal boundaries, the efficiency of the module is kept around 90 %, being the rest of energy transformed in heat generated by cells. Around 80 % of this heat energy is dissipated in the coolant when module is charged at 4C rate. This percentage is increased up to 95 % for slowest charging rate (1C). The rest of generated heat is transferred to the rest of module components.

Credit author statement

Alberto Broatch: Conceptualization, Methodology, Supervision, Reviewing. **Pablo Olmeda:** Formal Analysis, Investigation, Methodology. **Xandra Margot**: Formal Analysis, Supervision, Writing, Reviewing and Editing. **Luca Agizza**: Investigation, Software, Validation, Data curation, Writing-Original draft preparation. **Manuel Fernández**: Conceptualization, Methodology.

Declaration of competing interest

The authors declare that they have no known competing financial interests or personal relationships that could have appeared to influence the work reported in this paper.

Data availability

The data that has been used is confidential.

Acknowledgments

This work was supported by Generalitat Valenciana within the framework of the PROMETEO project “Contribution to the decarbonization of transport by optimizing the thermal management of vehicle batteries electrified” with reference number PROMETEO/2020/042. Luca Agizza is supported by grant ACIF/2021/005 funded by Conselleria de Innovación, Universidades, Ciencia y Sociedad Digital of the Generalitat Valenciana.

References

[1] Q. Hoarau, E. Lorang, An assessment of the European regulation on battery recycling for electric vehicles, Energy Policy 162 (2022) 112770.
[2] P. Slowik, A. Isenstadt, L. Pierce, S. Searle, Assessment of Light-Duty Electric Vehicle Costs and Consumer Benefits in the United States in the 2022–2035 Time Frame, 2022 (International Council on Clean Transportation).
[3] B.E. Lebrouhi, Y. Khattari, B. Lamrani, M. Maaroufi, Y. Zeraouli, T. Kousksou, Key challenges for a large-scale development of battery electric vehicles: a comprehensive review, Journal of Energy Storage 44 (2021) 103273.
[4] R. Faria, P. Marques, P. Moura, F. Freire, J. Delgado, A.T. De Almeida, Impact of the electricity mix and use profile in the life-cycle assessment of electric vehicles, Renew. Sustain. Energy Rev. 24 (2013) 271–287.
[5] J.A. Manzolli, J.P. Trovão, C.H. Antunes, A review of electric bus vehicles research topics–methods and trends, Renew. Sustain. Energy Rev. 159 (2022) 112211.
[6] M. Armand, P. Axmann, D. Bresser, M. Copley, K. Edström, C. Ekberg, H. Zhang, Lithium-ion batteries–current state of the art and anticipated developments, J. Power Sources 479 (2020) 228708.
[7] T.M. Bandhauer, S. Garimella, T.F. Fuller, A critical review of thermal issues in lithium-ion batteries, J. Electrochem. Soc. 158 (3) (2011) R1.
[8] A. Tomaszewska, Z. Chu, X. Feng, S. O’kane, X. Liu, J. Chen, B. Wu, Lithium-ion battery fast charging: a review, ETransportation 1 (2019) 100011.
[9] Agwu, D., Opara, F., Chukwuchekwa, N., Dike, D., & Uzoechi, L. (2017, November). Review of comparative battery energy storage system (BESS) for energy storage applications in tropical environment. In IEEE 3rd international conference on electro-Technology for National Development.
[10] J. Zhang, L. Zhang, F. Sun, Z. Wang, An overview on thermal safety issues of lithium-ion batteries for electric vehicle application, IEEE Access 6 (2018) 23848–23863.
[11] N. Piao, X. Gao, H. Yang, Z. Guo, G. Hu, H.M. Cheng, F. Li, Challenges and development of lithium-ion batteries for low temperature environments, eTransportation 11 (2022) 100145.
[12] M. Petzl, M. Kasper, M.A. Danzer, Lithium plating in a commercial lithium-ion battery–a low-temperature aging study, J. Power Sources 275 (2015) 799–807.
[13] Baghdadi, I., Briat, O., Eddahech, A., Vinassa, J. M., & Gyan, P. (2015, June). Electro-thermal model of lithium-ion batteries for electrified vehicles applications. In 2015 IEEE 24th international symposium on industrial electronics (ISIE) (pp. 1248-1252). IEEE.
[14] A. Jokar, B. Rajabloo, M. Désilets, M. Lacroix, Review of simplified Pseudo-two-dimensional models of lithium-ion batteries, J. Power Sources 327 (2016) 44–55.
[15] S. Nejad, D.T. Gladwin, D.A. Stone, A systematic review of lumped-parameter equivalent circuit models for real-time estimation of lithium-ion battery states, J. Power Sources 316 (2016) 183–196.
[16] A. Li, A.C.Y. Yuen, W. Wang, J. Weng, G.H. Yeoh, Numerical investigation on the thermal management of lithium-ion battery system and cooling effect optimization, Appl. Therm. Eng. 215 (2022) 118966.
[17] U. Morali, A numerical and statistical implementation of a thermal model for a lithium-ion battery, Energy 240 (2022) 122486.
[18] E. Jiaqiang, M. Yue, J. Chen, H. Zhu, Y. Deng, Zhu, Y.,& Kang, S., Effects of the different air-cooling strategies on cooling performance of a lithium-ion battery module with baffle, Appl. Therm. Eng. 144 (2018) 231–241.
[19] M. Akbarzadeh, T. Kalogiannis, J. Jaguemont, J. He, L. Jin, M. Berecibar, J. Van Mierlo, Thermal modeling of a high-energy prismatic lithium-ion battery cell and module based on a new thermal characterization methodology, Journal of Energy Storage 32 (2020) 101707.
[20] L.H. Saw, Y. Ye, A.A. Tay, W.T. Chong, S.H. Kuan, M.C. Yew, Computational fluid dynamic and thermal analysis of Lithium-ion battery pack with air cooling, Appl. Energy 177 (2016) 783–792.
[21] F. Bahiraei, A. Fartaj, G.A. Nazri, Electrochemical-thermal modeling to evaluate active thermal management of a lithium-ion battery module, Electrochim. Acta 254 (2017) 59–71.
[22] C. Zhao, W. Cao, T. Dong, F. Jiang, Thermal behavior study of discharging/charging cylindrical lithium-ion battery module cooled by channeled liquid flow, Int. J. Heat Mass Transf. 120 (2018) 751–762.
[23] Y.W. Pan, Y. Hua, S. Zhou, R. He, Y. Zhang, S. Yang, B. Wu, A computational multi-node electro-thermal model for large prismatic lithium-ion batteries, J. Power Sources 459 (2020) 228070.
[24] J. Wang, Y. Jia, N. Yang, Y. Lu, M. Shi, X. Ren, D. Lu, Precise equivalent circuit model for Li-ion battery by experimental improvement and parameter optimization, Journal of Energy Storage 52 (2022) 104980.
[25] Jeong, Y. M., Cho, Y. K., Ahn, J. H., Ryu, S. H., & Lee, B. K. (2014, September). Enhanced coulomb counting method with adaptive SOC reset time for estimating OCV. In 2014 IEEE energy conversion congress and exposition (ECCE) (pp. 1313-1318). IEEE.
[26] X. Li, Q. Wang, Y. Yang, J. Kang, Correlation between capacity loss and measurable parameters of lithium-ion batteries, Int. J. Electr. Power Energy Syst. 110 (2019) 819–826.
[27] Zhang, H., Mu, H. W., Zhang, Y., & Han, J. (2014). Calculation and characteristics analysis of lithium ion batteries' internal resistance using HPPC test. In advanced materials research (Vol. 926, pp. 915-918). Trans tech publications ltd.
[28] X. Wang, X. Wei, H. Dai, Estimation of state of health of lithium-ion batteries based on charge transfer resistance considering different temperature and state of charge, Journal of Energy Storage 21 (2019) 618–631.
[29] M.K. Tran, M. Mathew, S. Janhunen, S. Panchal, K. Raahemifar, R. Fraser, M. Fowler, A comprehensive equivalent circuit model for lithium-ion batteries, incorporating the effects of state of health, state of charge, and temperature on model parameters, Journal of Energy Storage 43 (2021) 103252.
[30] D. Kang, P.Y. Lee, K. Yoo, J. Kim, Internal thermal network model-based inner temperature distribution of high-power lithium-ion battery packs with different shapes for thermal management, Journal of Energy Storage 27 (2020) 101017.
[31] A. Nazari, S. Farhad, Heat generation in lithium-ion batteries with different nominal capacities and chemistries, Appl. Therm. Eng. 125 (2017) 1501–1517.
[32] A. Broatch, P. Olmeda, X. Margot, L. Agizza, A generalized methodology for lithium-ion cells characterization and lumped electro-thermal modelling, Appl. Therm. Eng. 217 (2022) 119174.
[33] J. Peng, J. Meng, D. Chen, H. Liu, S. Hao, X. Sui, X. Du, A review of Lithium-ion battery capacity estimation methods for onboard battery management systems: recent Progress and perspectives, Batteries 8 (11) (2022) 229.
[34] H. Wang, S. Frisco, E. Gottlieb, R. Yuan, J.F. Whitacre, Capacity degradation in commercial Li-ion cells: the effects of charge protocol and temperature, J. Power Sources 426 (2019) 67–73.
[35] N. Omar, P. Van den Bossche, T. Coosemans, J. Van Mierlo, Peukert revisited—critical appraisal and need for modification for lithium-ion batteries, Energies 6 (11) (2013) 5625–5641.
[36] D. Wycisk, G.K. Mertin, M. Oldenburger, A. Latz, Analysis of heat generation due to open-circuit voltage hysteresis in lithium-ion cells, Journal of Energy Storage 61 (2023) 106817.
[37] T. Zheng, J.R. Dahn, Hysteresis observed in quasi open-circuit voltage measurements of lithium insertion in hydrogen-containing carbons, J. Power Sources 68 (2) (1997) 201–203.
[38] Zhang, R., Xia, B., Li, B., Lai, Y., Zheng, W., Wang, H., & Wang, M. (2018). Study on the characteristics of a high capacity nickel manganese cobalt oxide (NMC) lithium-ion battery—an experimental investigation. Energies, 11(9), 2275.
[39] Christophersen, J. P. (2015). Battery test manual for electric vehicles, revision 3 (no. INL/EXT-15-34184). Idaho National lab.(INL), Idaho Falls, ID (United States).
[40] L. Zhang, H. Peng, Z. Ning, Z. Mu, C. Sun, Comparative research on RC equivalent circuit models for lithium-ion batteries of electric vehicles, Appl. Sci. 7 (10) (2017) 1002.
[41] H.M. Cho, W.S. Choi, J.Y. Go, S.E. Bae, H.C. Shin, A study on time-dependent low temperature power performance of a lithium-ion battery, J. Power Sources 198 (2012) 273–280.

[42] M. Steinhardt, E.I. Gillich, A. Rheinfeld, L. Kraft, M. Spielbauer, O. Bohlen, A. Jossen, Low-effort determination of heat capacity and thermal conductivity for cylindrical 18650 and 21700 lithium-ion cells, Journal of Energy Storage 42 (2021) 103065.
[43] M. Koller, J. Unterkofler, G. Glanz, D. Lager, A. Bergmann, H. Popp, Radial thermal conductivity measurements of cylindrical Lithium-ion batteries—an uncertainty study of the pipe method, Batteries 8 (2) (2022) 16.
[44] S. Yang, C. Ling, Y. Fan, Y. Yang, X. Tan, H. Dong, A review of lithium-ion battery thermal management system strategies and the evaluate criteria, Int. J. Electrochem. Sci. 14 (7) (2019) 6077–6107.
[45] P. Sliwinski, P. Patrosz, Methods of determining pressure drop in internal channels of a hydraulic motor, Energies 14 (18) (2021) 5669.
[46] E.N. Sieder, G.E. Tate, Heat transfer and pressure drop of liquids in tubes, Industrial & Engineering Chemistry 28 (12) (1936) 1429–1435.
[47] N. Collath, B. Tepe, S. Englberger, A. Jossen, H. Hesse, Aging aware operation of lithium-ion battery energy storage systems: a review, Journal of Energy Storage 55 (2022) 105634.
[48] A. De Vita, A. Maheshwari, M. Destro, M. Santarelli, M. Carello, Transient thermal analysis of a lithium-ion battery pack comparing different cooling solutions for automotive applications, Appl. Energy 206 (2017) 101–112.
[49] L.H. Saw, Y. Ye, A.A.O. Tay, Electro-thermal analysis and integration issues of lithium-ion battery for electric vehicles, Appl. Energy 131 (2014) 97–107.
[50] S. Chen, N. Bao, X. Peng, A. Garg, Z. Chen, A thermal design and experimental investigation for the fast-charging process of a lithium-ion battery module with liquid cooling, Journal of Electrochemical Energy Conversion and Storage 17 (2) (2020).
[51] R. Gozdur, B. Guzowski, Z. Dimitrova, A. Noury, G. Mitukiewicz, D. Batory, An energy balance evaluation in lithium-ion battery module under high temperature operation, Energ. Conver. Manage. 227 (2021) 113565.